Radiation-enhanced fission track annealing revisited and consequences for apatite thermochronometry

Kalin T. McDannell[1*], Dale R. Issler[1], and Paul B. O'Sullivan[2]

[1]*Geological Survey of Canada, Natural Resources Canada, 3303 33 St. NW, Calgary, AB, T2L 2A7 Canada*

[2]*GeoSep Services, 1521 Pine Cone Rd., Moscow, ID, 83843 United States*

[*]Corresponding author: kalin.mcdannell@canada.ca

ABSTRACT

Apatite fission track (AFT) analyses for granitoid and metamorphic bedrock samples from the Western Superior Province (Ontario), the Churchill-Rae Province (Melville Peninsula and Southampton Island, Nunavut), and the Slave Province (Northwest Territories) show a broad range of single grain effective uranium concentrations (eU) (<1 to ~300 ppm) and some of the oldest reported AFT ages in North America. Although most of our samples have a typical fluorapatite composition (effective Cl < 0.1 apfu) with implied low track retentivity, single grain AFT ages are overdispersed and decrease with increasing eU content. This eU-age relationship is resonant of the Hendriks and Redfield (*Earth and Planetary Science Letters*, 236, 443-458, 2005) argument for α-radiation enhanced fission track annealing (REA) and is analogous to the negative age-eU correlation observed in published zircon and titanite (U-Th)/He data from slowly-cooled cratonic rocks. The high intra-sample age variability for low-Cl bedrock apatites with protracted histories (>200-500 m.y.) at <100°C since the Precambrian suggests strong REA control on AFT ages. Conversely, some low Cl AFT samples with a narrower eU range show less age dispersion and a weak apparent age-eU correlation. A complex trade-off between radiation damage and chemical composition (e.g. low Cl and REE enrichment) is implied when eU and r_{mr0} (and equivalent effective Cl) are correlated. In all cases, the samples fail the canonical χ^2 test to evaluate if grains are from a single age population (χ^2 <5%) and have characteristic "open jaw" radial plots, generally considered to indicate multiple age populations. Previous assessments of the influence of REA on AFT age were based on evaluating central age and mean track length, which potentially mask high single-grain age scatter and REA effects. Therefore, it is crucial that bedrock samples exhibiting high age scatter are evaluated in terms of intra-sample compositional heterogeneity. AFT samples with relatively low Cl concentrations are especially prone to greater REA control of cooling ages and this underscores the need for routine acquisition of compositional data for AFT datasets. Our broad range in single-grain AFT ages (with no other clear, strong compositional controls) supports the notion that radiation damage affects both the AFT and (U-Th)/He thermochronometers in slowly-cooled settings and must be accounted for during thermal history modeling and interpretation.

Keywords: apatite; fission track; alpha damage; radiation-enhanced annealing; uranium

1. Introduction

The fission-track dating method is based on the accumulation of crystallographic damage trails due to spontaneous nuclear fission of ^{238}U in U-bearing minerals such as apatite $Ca_5(PO_4)_3(OH,F,Cl)$ (Price and Walker, 1963; Wagner, 1968; Naeser and Faul, 1969). Apatite fission track (AFT) thermochronology is based on the principle that crystal damage is partially or completely annealed or "healed" at elevated temperature, which results in a quantifiable reduction to track lengths and densities (e.g. Gleadow and Duddy, 1981; Green, 1988). However, difficulties remain in fully characterizing the thermally-activated annealing behaviour of fission tracks and the temperature of complete track annealing, as these factors are influenced by duration of heating (e.g. Green et al., 1986; Green, 1988; Green et al., 1989), variable apatite composition (i.e. common fluorapatite vs. chlorapatite; Carlson, 1990; Carlson et al., 1999; Barbarand et al., 2003), and crystal anisotropy (e.g. Donelick et al., 1999; Ketcham et al., 2007; Nadzri et al., 2017). Chlorine content is considered the dominant compositional control on fission-track retentivity, along with other secondary Ca-site (substituting) cations, such as Fe, Na, Mn, and S, and some rare-earth elements such as La, Ce, and Y (Carlson et al., 1999; Barbarand et al., 2003; Donelick et al., 2005). However, the trade-offs between kinetic variability, elemental substitutions, and track annealing behaviour are multifaceted and not fully understood (Ketcham et al., 1999; Barbarand et al., 2003).

The primary spontaneous decay process during ^{238}U decay in apatite is ^{4}He α-particle emission (Donelick et al., 2005 for review). Alpha-recoil damage acts to diminish fission-track stability in U-bearing phases such as zircon (Kasuya and Naeser, 1988), titanite (Lumpkin et al., 1991), and apatite (Ritter and Märk, 1986). Extreme α-damage levels cause crystallographic amorphization in zircon due to relatively high U content (Chakoumakos et al., 1987; Murakami et al., 1991; Nasdala et al., 2001), whereas α-damage is recoverable in apatite (Weber et al., 1997; Li et al., 2017). Alpha-damage annealing has long been considered analogous to fission track annealing behaviour (e.g. Flowers et al., 2009; Gautheron et al., 2009), however it has been previously proposed that α-damage annealing is slower than fission-track annealing (Ritter and Märk, 1986; Fox and Shuster, 2014). Moreover, experiments comparing synthetic apatite (no α-damage) and natural apatites demonstrate that the α-damage present in natural samples acts to enhance fission track annealing (Carpena and Lacout, 2010). Alpha-damage also has consequences for He

diffusion in apatite (U-Th)/He (AHe) thermochronometry (e.g. Farley et al., 1996; Gautheron et al., 2009; Ketcham et al., 2017; Recanati et al., 2017). There is now a better understanding of the numerous factors affecting He diffusivity in apatite including, compositional and crystallographic controls on α-damage annealing (Gautheron et al., 2009; Djimbi et al., 2015), strain-induced dislocation traps (McDannell et al., 2018), crystallographic microvoids (Zeitler et al., 2017), and vacancy damage (Gerin et al., 2017). These radiation damage effects manifest in apatite by cumulative damage increasing He retentivity and have been explored and described through models of diffusive loss (Shuster et al., 2006; Flowers et al., 2009; Gautheron et al., 2009; Gerin et al., 2017; Willett et al., 2017).

Radiation damage is often discussed in terms of "alpha dose," which is a quantitative estimate of the self-irradiation (driven by the α-fluence) in a mineral and the damage accumulated over some ingrowth time (e.g. Nasdala et al., 2001). The first-order control on α-damage is U content, or "effective U" concentration (eU=U+0.235×Th+0.0046×Sm) of the host grain weighted for parent α-productivity. For any mineral exhibiting a diffusive relationship with α-dose it is expected that a positive age-eU correlation exists at low dose and a negative relationship is evident after the damage percolation threshold (or point at which damage interconnects) is reached because of increased diffusivity. For example, an α-damage model has been developed for zircon where there is an expected, subtle decrease in ^{4}He diffusivity (increased retentivity) at low α-dose and then an increase in diffusivity at high α-dose (Guenthner et al., 2013). Guenthner et al. (2013) demonstrated that for He diffusion in zircon the relationship between age and eU is strongly influenced by thermal history. A negative age-eU relationship should become apparent in grains that have spent prolonged periods below the partial retention zone for He (Guenthner et al., 2013). A similar relationship between age and α-dose has been observed in highly-damaged titanite (Baughman et al., 2017; Guenthner et al., 2017), however no damage model yet exists that adequately predicts a negative age-eU trend for apatite (U-Th)/He data under prolonged slow-cooling conditions. This may change, as the He diffusion percolation threshold for α-damage has been recently described in apatite (Ketcham et al., 2017; Recanati et al., 2017), and seems (at least somewhat) genetically similar to damage modes in zircon and titanite, albeit orders of magnitude lower and more easily recoverable (e.g. Li et al., 2017).

These new developments in understanding how α-damage acts to modify He diffusion are integral for using apatite as a viable thermochronometer and undoubtedly have implications for AFT analysis and fission-track retention in rocks that have experienced slowly-cooled histories. The relatively subtle kinetic and compositional controls on apatite annealing and retentivity in rapidly-cooled settings become more complex and magnified in cratonic interiors (e.g. Green and Duddy, 2006; Flowers, 2009). There have been many problems associated with the interpretation of both AFT and AHe data in slowly-cooled settings, including significant intra- and inter-sample age dispersion (e.g. Fitzgerald et al., 2006; McKeon, 2012; McDannell et al., 2018) and AFT<AHe cooling age inversion (e.g. Hendriks and Redfield, 2005; Green et al., 2006; Flowers and Kelley, 2011). Hendriks and Redfield (2005) suggested that elevated U concentration in apatite has a strong influence on fission-track annealing; invalidating prior thermochronologic interpretations for cooling signals across the Fennoscandian Shield. In a series of papers, this matter and the robustness of AFT versus AHe dating was debated (Green and Duddy, 2006; Hendriks and Redfield, 2006; Larson et al., 2006). The apparent U control on AFT ages was largely dismissed as being due to lithologic differences and elevated Cl content in the analysed apatites (Kohn et al., 2009). Hendriks and Redfield's argument for AHe dates being more reliable than AFT ages was contested and attributed to variability in He retentivity, rather than variability in AFT annealing behaviour (Green et al., 2006).

However, the effect of eU on AFT ages was perhaps dismissed prematurely, and analytical advances in the past 15 years have motivated changes in AFT methodology to better address this problem. The potential relationship between U and AFT age has long been recognized and an early example of a negative correlation between zircon FT age and U concentration is given in Carter (1990) using the external detector method (EDM). Discussion around this relationship is focused on single-grain U variability, track density, and potential counting biases, as well as the fact that both AFT age and U estimates are derived from the same induced track count, and therefore related. The recommendation in Carter (1990) for determining if a real association exists between age and U is to measure U independently. The introduction of laser ablation inductively coupled plasma mass spectrometry (LA-ICP-MS) for AFT dating (Hasebe et al., 2004) made the direct measurement of U procedurally advantageous over the external detector method (EDM), which uses an irradiated, low-U muscovite detector as a proxy for apatite ^{238}U

content through reactor-induced fission tracks. The main drawback for ICP-MS ^{238}U measurement is that very low U content (<< 0.5 ppm) is difficult to measure and leads to modestly older ages compared to the EDM (Seiler et al., 2013), nonetheless U can still be reliably measured at <1 ppm. It is also well established that apatites with high fission-track density (i.e. old grains or high U) are more difficult to measure using the EDM, consequently biasing AFT measurements towards younger or low U grains (e.g. Carter, 1990; Seiler et al., 2013). In a series of analyses on laboratory age standard AFT grains, Hasebe et al. (2004) showed that the EDM underestimated the U content of high U, whole-grain laboratory age standard apatites with respect to LA-ICP-MS measurements.

In light of advances in precise, *in situ* U concentration measurements for AFT analysis, re-evaluation of α-radiation enhanced annealing (REA) is warranted. Assessing the viability of REA in slowly-cooled terranes is important for the understanding of the annealing kinetics of apatite fission tracks and the implications for other thermochronometers that are affected by the same α-damage and annealing processes, such as the case with the apatite (U-Th)/He system (Gautheron et al., 2013; Recanati et al., 2017). We present new LA-ICP-MS AFT data from Archean-Paleoproterozoic plutonic granitoids and gneissic bedrock samples from localities across the Canadian Shield and assess the REA potential related to U content. Grains that are characterized by highly variable eU and low Cl concentrations (<0.1 atom per formula unit, apfu) typically show a strong, negative age-eU correlation, whereas contrasting metasedimentary samples from southern Baffin Island with "typical apatite" eU levels (less variability, ~20-30 ppm) and low Cl (<0.1 apfu) show seemingly weak U control on age, less single-grain age scatter, or display complex relationships between retentivity proxies (i.e. eU, r_{mr0}, and effective Cl).

Our intent is not aimed at generating a calibrated model of REA behaviour, nor wholly reconciling observations between AFT and AHe single-grain ages in slowly-cooled settings for geologic interpretation – but rather to bring REA back into the communal foreground and assert that this phenomenon exists, although it is poorly understood due to compositional complexities associated with fission-track annealing.

2. Regional Geologic Setting

The AFT samples presented here all come from exposed granitic and gneissic bedrock across Canada. An overview of the Precambrian geologic history of the Canadian Shield is provided by Hoffman et al. (1989) and here we focus mainly on areas of Archean (>2.5 Ga) crust that are currently exposed across the Canadian interior that were sutured during Trans-Hudson orogenesis and Laurentia assembly at ca. 1.9-1.8 Ga. The major terranes that were sampled are the Western Superior Province (Percival et al., 2012), rocks of the northeastern Churchill Province-Rae domain at Southampton Island (Berman et al., 2013) and Melville Peninsula (Berman et al., 2015), and the Slave Province (Isachsen and Bowring, 1994) all shown on figure 1. Results from southern Baffin Island are also shown for comparison to the aforementioned data (see discussion).

The Archean-Proterozoic tectonomorphic history and setting for each terrane is thoroughly described in their respective reference. All of these regions have presumably been exposed at near surface conditions or in the upper crust since the mid-late Proterozoic and experienced minor, episodic burial throughout the Phanerozoic (Burgess, 2008; Miall and Blakey, 2008). The Archean-Paleoproterozoic age of these terranes and the limited Phanerozoic sedimentary strata provide few constraints on the burial and exhumation history of these rocks. The Phanerozoic sedimentary succession in central Canada is preserved in Hudson Bay (mainly Paleozoic, ~2500 m thick; fig 1.) and unconformably overlies Canadian Shield bedrock (Pinet et al., 2013). The Paleozoic platform sequence is exposed in the Western Superior Province at Hudson and James Bay, and Ordovician-Silurian sediments onlap much of the southern Arctic, northern Melville Peninsula (Corrigan et al., 2013), and Baffin Island bedrock (fig. 1).

In the absence of formal models for the time-temperature history of many of these areas, geologic evidence and the sparse Phanerozoic sedimentary record yield clues about the thermal history experienced by Shield rocks. Kimberlites can include sedimentary xenolith evidence of the pre-existing Paleozoic cover that was removed by erosion. The Jericho kimberlites in the central Slave craton have limestone xenoliths of Middle Devonian age (L. Eifelian-E. Givetian) (Cookenboo et al., 1998) and the ca. 75-45 Ma Lac de Gras kimberlite field suggests up to ~1.4 km of Cretaceous strata existed at that time (Nassichuk and McIntyre, 1995; Stasiuk et al., 2006). The Mesozoic Kirkland Lake (Ontario) kimberlites contain Ordovician-Devonian xenoliths in

the Superior Province (McCracken et al., 2000) and the Jurassic Chidliak kimberlites of southern Baffin Island also contain Late Ordovician-Early Silurian xenoliths (Zhang and Pell, 2014). These areas all indicate that most of interior Canada was inundated by a shallow sea in the middle Paleozoic and experienced some level of regionally cohesive burial and exhumation through Paleozoic-Mesozoic time, which is reinforced by regional studies using low-temperature thermochronology (Ault et al., 2009; Feinstein et al., 2009). AFT studies suggest that most of the Trans-Hudson region remained at <80-90°C since the Ordovician (Pinet et al. 2016) and that rocks of the Superior Province in Ontario were never hotter than ~90°C during episodic burial and exhumation since the Cambrian (Kohn et al., 2005). Generally speaking, the majority of the Canadian Shield has been at temperatures ≤100°C at least since the latest Precambrian-Cambrian (>500 Ma).

3. Analytical Methods

3.1 LA-ICP-MS apatite fission track analysis

AFT ages were determined using the LA-ICP-MS method (Hasebe et al. 2004; Donelick et al. 2005; Chew and Donelick 2012), which gives similar results to the traditional external detector method but avoids the requirement for sample irradiation in a nuclear reactor (Seiler et al., 2013). A single grain mount was used to acquire AFT age, length and D_{par} data for each sample according to the procedures described in Donelick et al. (2005). Length and D_{par} data are not presented here and will be discussed in future publications. Following mineral separation procedures, apatite separates were mounted in epoxy, polished, and etched in 5.5M HNO_3 for 20s at 21˚C to reveal all natural fission tracks intersecting the polished grain surface. For each age grain, locations were recorded and spontaneous AFT densities were counted using a microscope at 2000x magnification under unpolarized light. ^{238}U concentrations were determined for the track count areas on each age grain using the Washington State University (WSU) Finnigan Element II Magnetic Sector ICP-MS by measuring the weighted mean ratio of ^{238}U to ^{43}Ca from multiple spot analyses at a fixed laser point (^{232}Th and ^{147}Sm were also measured). The volume of ablated material is estimated using ^{43}Ca assuming that Ca occurs in stoichiometric amounts. AFT ages were calculated using the LA-ICP-MS zeta calibration approach (Donelick et al., 2005; Vermeesch, 2017) based on the Durango apatite age standard. Apatite U-Pb age data were acquired for AFT age grains as described in Chew and Donelick (2012). Apatite U-Pb age

density plots were created using DensityPlotter v. 8.2 software (Vermeesch, 2012) using a Kernel Density Estimator with an adaptive bandwidth and logarithmic transformation of the single-grain ages and their 2σ errors. The quoted "mixture model" ages incorporate all measured ages and are for a single age population.

3.2 Apatite elemental analyses and the effective Cl kinetic parameter

Sample apatite grains were analysed for 13 elements (F, Na, Mg, P, S, Cl, Ca, Mn, Fe, Sr, Y, La, and Ce) using the WSU JEOL JXA8500F Field Emission Electron Microprobe operated at 15 kV (20 nA current) with a beam size of 5 μm. Laboratory weight % oxide values were converted to atom per formula unit (apfu) values, including estimation of OH content from Cl and F values, using the apatite stoichiometric model of Ketcham (2015). The r_{mr0} kinetic parameter was calculated for each analysed apatite grain by substituting the apfu values into the multivariate equation of Carlson et al. (1999). The nonlinear r_{mr0} values were converted into "effective" Cl values (apfu) using the empirical r_{mr0}-Cl relation of Ketcham et al. (1999) for better visualization of data on a linear scale, for calculating arithmetic means of single-grain kinetic parameters, and for comparison with the commonly used single kinetic parameter, Cl content. In the majority of our samples, measured Cl and D_{par} show no relation with AFT age and in general, effective Cl is preferred as a kinetic parameter over measured Cl because it takes into account the contribution of multiple elements that influence track retentivity. Negative effective Cl values ($r_{mr0} > 0.84$) indicate that AFT track retentivity is lower than that of the apatite used for the laboratory annealing experiments (Ketcham et al., 1999). We use the Carlson et al. (1999) r_{mr0} equation rather than the Ketcham et al. (2007) equation because in our experience with multi-kinetic AFT populations the former generally produces a broader range of r_{mr0} values than the latter equation for apatite samples showing a range of kinetic behavior. The greater spread in values can result in better definition of age populations. Ketcham et al. (2007) demonstrates that both experimental datasets can be reconciled but this does not necessarily mean that the Ketcham et al. (2007) equation is superior or more accurate. Refitting of the model parameters in the newer equation may be influenced by: (1) the narrower compositional range of the Barbarand et al. (2003) experimental apatite compared with those of Carlson et al. (1999), which may be biasing the fit due to the overriding influence of Cl and (2) there may be residual analyst bias between experiments even after corrections were applied.

4. Apatite fission track results

We present new LA-ICP-MS AFT results for 11 samples taken from cratonic bedrock across the Canadian interior (table 1). Two other samples from Baffin Island are from Paleoproterozoic metasediments overlying Archean basement that have internally consistent apatite U-Pb ages and are treated as homogeneous samples (i.e. not detrital). There is also an additional AFT sample with accompanying AHe data previously published for the Hudson Bay region in Pinet et al. (2016) that is examined in the discussion (see table 1). Other published AFT data from Canada are included for comparison only to illustrate other types of complex relationships between AFT single-grain age, eU/α-dose, and other kinetic parameters. A plot of central AFT age/MTL versus eU is shown in figure 2. This visualization of AFT data (generally utilizing ^{238}U only) has been the convention for previous studies addressing REA (e.g. Hendriks and Redfield, 2005; Kohn et al., 2009). All of our samples fail the chi-squared test and have characteristic open-jaw radial plots indicative of high age dispersion (fig. 3). This is a typical feature of detrital AFT data due to variable provenance and composition; however for bedrock samples this is explained only by slow cooling and amplified compositional effects. An interesting facet of the data are that samples with fewer grains typically have much lower dispersion (fig. 3), which is probably a result of "under-sampling" and is an issue that may be unwittingly pervasive in older vintage datasets from slowly-cooled terrains.

4.1 Western Superior Province

Sample PBA-98-743 is from a biotite tonalite-gneiss in the Harmon Lake Gneiss Complex of the Wabigoon Subprovince. The gneiss has a mean $^{207}Pb/^{206}Pb$ zircon core metamorphic protolith age of 2890 ± 8 Ma (MSWD=1.1) and a U-Pb titanite age of 2678 ± 2 Ma (Percival et al., 2004). The corresponding sample apatite U-Pb mixture model single age peak is 2971 ± 174 Ma (2σ; n=25). The AFT sample has a pooled age of 572.3 ± 15.6 Ma (1σ; n=40) and a central age of 597 ± 37 (1σ) with 36% age dispersion. The mean track length (MTL) is 12.07 ± 1.94 μm (1σ; n=130). The mean kinetic parameters for PBA-98-743 are: measured D_{par} of 1.89 μm, eU of 7 ppm (range 1-19 ppm), calculated r_{mr0} of 0.84, and measured Cl of 0.008 apfu.

Sample 03-GRS-013 is from a tonalite-quartz diorite in the Mesoarchean Sachigo Subprovince. The apatite U-Pb mixture model single age peak is 3009 ± 94 Ma (2σ; n=29). The AFT sample has a pooled age of 414.0 ± 14.1 Ma (1σ; n=40) and a central age of 447 ± 34 (1σ) with 46% age dispersion. The MTL is 12.51 ± 1.63 μm (1σ; n=131). The mean kinetic parameters for 03-GRS-013 are: measured D_{par} of 1.91 μm, eU of 33 ppm (range 1-241 ppm), calculated r_{mr0} of 0.84, and measured Cl of 0.003 apfu.

4.2 Slave Province

Sample 12-DRA03-001 is from a plagioclase-bearing porphyritic intrusion with a turbidite deposit near Wheeler Lake in the Northwest Territories. This sample is at the approximate location of the Isachsen and Bowring (1994) lithic tuff sample (within turbidites) that has a reported U-Pb age of 2612 ± 1 Ma. The sample apatite U-Pb mixture model single age peak is 2628 ± 96 Ma (2σ; n=36). The AFT sample has a pooled age of 335.7 ± 11.3 Ma (1σ; n=40) and a central age of 344 ± 14 (1σ) with 22% age dispersion. The MTL is 12.04 ± 2.39 μm (1σ; n=131). The mean kinetic parameters for 12-DRA03-001 are: measured D_{par} of 1.87 μm, eU of 16 ppm (range 2-55 ppm), calculated r_{mr0} of 0.83, and measured Cl of 0.019 apfu.

Sample BNB97-035 is plutonic med-coarse grained biotite granitoid with strong lineations taken from the west flank of the Sleepy Dragon Complex in the Yellowknife Domain of the Slave craton with nearby basement crystallization ages of ca. 2900 Ma (Bleeker et al., 1999), similar to the sample apatite U-Pb mixture model single age peak of 2858 ± 124 Ma (2σ; n=22). The AFT sample has a pooled age of 229.3 ± 22.1 Ma (1σ; n=40) and a central age of 272 ± 16 (1σ) with 34% age dispersion. The MTL is 12.75 ± 1.80 μm (1σ; n=116). The mean kinetic parameters for BNB97-035 are: measured Dpar of 1.72 μm, eU of 21 ppm (range 0.2-98), calculated r_{mr0} of 0.85, and measured Cl of 0.006 apfu.

Sample 12NK-L18A3 is from granitic gneiss in Nunavut with a zircon U-Pb age of 2487 ± 5.4 Ma and a metamorphic overprint U-Pb age of 2377 ± 3.5 Ma (Davis et al., 2014). The apatite U-Pb mixture model single age peak is significantly younger at 1788 ± 40 Ma (2σ; n=24). The AFT sample has a pooled age of 392.4 ± 9.0 Ma (1σ; n=26) and a central age of 397 ± 13 (1σ) with 14% age dispersion. The MTL is 11.91 ± 2.06 μm (1σ; n=78). The mean kinetic parameters for 12NK-L18A3 are: measured Dpar of 1.85 μm, very high eU of 339 ppm (range 139-655), calculated r_{mr0} of 0.79, and measured Cl of 0.012 apfu.

4.3 Churchill-Rae Province, Melville Peninsula region

Sample SNB-01-M2055 is from Melville Peninsula, ~150 km southwest of Committee Bay and is a foliated biotite tonalite that cuts a komatiite at the base of the Howling Wolf section with an U-Pb zircon igneous crystallization age of 2606 ± 4 Ma (Cairns et al., 2005). The apatite U-Pb mixture model single age peak is 1940 ± 68 Ma (2σ; n=26). The AFT sample has a pooled age of 348.5 ± 9.8 Ma (1σ; n=30) and a central age of 356 ± 18 (1σ) with 24% age dispersion. The MTL is 12.19 ± 2.30 μm (1σ; n=130). The mean kinetic parameters for SNB-01-M2055 are: measured D_{par} of 2.00 μm, eU of 14 ppm (range 0.2-46 ppm), calculated r_{mr0} of 0.84, and measured Cl of 0.003 apfu.

Sample 10CXAD-086A is from eastern Melville Peninsula on the Foxe Basin margin and was collected from a plutonic gabbro-anorthosite with nearby detrital U-Pb ages of 1899 ± 7 Ma and 1897 ± 15 Ma in the overlying Paleoproterozoic Penrhyn Group (Partin et al., 2014). The sample apatite U-Pb mixture model single age peak is 1803 ± 73 Ma (2σ; n=24). The AFT sample has a pooled age of 363.1 ± 28.5 Ma (1σ; n=40) and a central age of 460 ± 44 (1σ) with 57% age dispersion. The MTL is 12.60 ± 1.79 μm (1σ; n=132). The mean kinetic parameters for 10CXAD-086A are: measured D_{par} of 2.12 μm, eU of 13 ppm (range 0.2-73 ppm), calculated r_{mr0} of 0.82, and measured Cl of 0.029 apfu.

Sample 13LVA04 is from a gabbro at the Discovery outcrop that cuts a banded iron formation and the Sam Fm. at the Thelon Basin in S. Nunavut. The apatite U-Pb mixture model single age peak is 2224 ± 125 Ma (2σ; n=39). The AFT sample has a pooled age of 546.0 ± 33.8 Ma (1σ; n=40) and a central age of 557 ± 31 (1σ) with 21% age dispersion. The MTL is 12.44 ± 2.06 μm (1σ; n=121). The mean kinetic parameters for 13LVA04 are: measured D_{par} of 1.92 μm, eU of 7 ppm (range 3-42 ppm), calculated r_{mr0} of 0.80, and measured Cl of 0.012 apfu.

Sample 09SZ-23-01 is from Precambrian granitic gneiss at the northern margin of Melville Peninsula at the Fury and Hecla Strait, <200 m from the Paleozoic unconformity presented in Pinet et al. (2016). The AFT sample has a pooled age of 462.7 ± 29.9 Ma and a central age of 486 ± 27 Ma with 21% age dispersion. The MTL is 12.18 ± 1.58 μm (1σ; n=100). The mean kinetic parameters for 09SZ-23-01 are: measured D_{par} of 1.67 μm, ^{238}U of 6 ppm (range 3-12 ppm), calculated r_{mr0} of 0.85, and measured Cl of 0.016 apfu. There are no apatite U-Pb data for this sample but there are coexisting apatite (U-Th)/He data with a weighted mean age of 347 ±

65 Ma (1σ; n=5) and an additional nearby (U-Th)/He sample 09SZ-24-01 with a weighted mean age of 211 ± 80 Ma (1σ; n=7). Sample 09SZ-23-01 is not entirely comparable to our ICP-MS AFT data because only ^{238}U was measured and is not necessarily representative of the eU, as Th and Sm contributions could make the eU much greater and add greater variability between grains. To add more approximate values for eU we took the average Th and Sm concentrations of the two apatite (U-Th)/He samples and used those to calculate eU for the AFT data. This yields a mean eU of 14 ppm (range 11-20 ppm). Further information regarding AFT analytical methods, compositional data, and accompanying AHe data (sample 09SZ-24-01 at about the same location) is given in Lavoie et al. (2013) and Pinet et al. (2016).

4.4 Churchill-Rae Province, Southampton Island

Sample 07CYA-M38B is from gabbroic anorthosite bedrock on Southampton Island with a U-Pb zircon inherited primary crystallization age of 3005 ± 22 Ma and a recrystallization age of 1870 ± 10 Ma (MSWD=1.2) due to Trans-Hudson overprinting (Rayner et al., 2011). The apatite U-Pb mixture model single age peak is 1834 ± 60 Ma (2σ; n=35). The AFT sample has a pooled age of 341.6 ± 10.5 Ma (1σ; n=40) and a central age of 384 ± 21 (1σ) with 30% age dispersion. The MTL is 12.22 ± 2.0 μm (1σ; n=132). The mean kinetic parameters for 07CYA-M38B are: measured D_{par} of 1.90 μm, eU of 22 ppm (range 1-71 ppm), calculated r_{mr0} of 0.84, and measured Cl of 0.024 apfu.

Sample 07CYA-M133A is a plutonic diorite from Southampton Island with a U-Pb igneous crystallization age of 1842 ± 5 Ma (Rayner et al., 2011). The apatite U-Pb mixture model single age peak is 1812 ± 79 Ma (2σ; n=13). The AFT sample has a pooled age of 364.2 ± 10.6 Ma (1σ; n=15) and a central age of 375 ± 17 (1σ) with 16% age dispersion. The MTL is 11.57 ± 2.16 μm (1σ; n=101). The mean kinetic parameters for 07CYA-M133A are: measured D_{par} of 2.26 μm, eU of 74 ppm (range 7-258 ppm), calculated r_{mr0} of 0.80, and measured Cl of 0.086 apfu.

4.5 Rae craton, southern Baffin Island

Sample 09SRB-M100 is a metasedimentary semipelite within the Paleoproterozoic Hoare Bay Group at Kumlien Fiord on the Cumberland Peninsula, Baffin Island. The apatite U-Pb mixture model single age peak is 1674 ± 35 Ma (2σ; n=28). The AFT sample has a pooled age of 97.2 ± 4.3 Ma (1σ; n=35) and a central age of 102 ± 8 (1σ) with 37% age dispersion. The MTL is 12.94

± 2.23 μm (1σ; n=41). The mean kinetic parameters for 09SRB-M100 are: measured D_{par} of 2.14 μm, eU of 22 ppm (range 1-69 ppm), calculated r_{mr0} of 0.83, and measured Cl of 0.023 apfu.

Sample 14SUB-H43A is a metamorphic garnet-biotite psammite from a Paleoproterozoic metasediment/layered mafic intrusion sequence on northern Hall Peninsula, Baffin Island. The apatite U-Pb mixture model single age peak is 1782 ± 38 Ma (2σ; n=25). The AFT sample has a pooled age of 440.2 ± 11.4 Ma (1σ; n=25) and a central age of 442 ± 12 (1σ) with 10% age dispersion. The MTL is 12.46 ± 1.72 μm (1σ; n=130). The mean kinetic parameters for 14SUB-H43A are: measured D_{par} of 2.29 μm, eU of 26 ppm (range 16-35 ppm), calculated r_{mr0} of 0.82, and measured Cl of 0.022 apfu.

4.6 Grenville Orogen, southeast Quebec

Sample 02NKL-871 is from a granitic orthogneiss in southeast Quebec. It is shown here for comparative purposes, as it is much younger (Grenvillian) than the majority of our other samples taken from Archean bedrock. The apatite U-Pb mixture model single age peak is 951 ± 38 Ma (2σ; n=25). The AFT sample has a pooled age of 160.8 ± 4.5 Ma (1σ; n=35) and a central age of 177 ± 13 (1σ) with 38% age dispersion. The MTL is 12.27 ± 1.80 μm (1σ; n=135). The mean kinetic parameters for 02NKL-871 are: measured D_{par} of 1.83 μm, eU of 31 ppm (range 2-160 ppm), calculated r_{mr0} of 0.85, and measured Cl of 0.008 apfu. This sample will also be discussed with the Anticosti Island sample of Powell et al., (2018a).

5. Discussion

5.1 AFT age relationships between kinetic parameters eU, effective Cl, and r_{mr0}

Using plots of central age versus U, Hendriks and Redfield (2005) proposed that REA could explain the observed decrease in AFT age with increasing U content for samples from the Fennoscandian Shield. Kohn et al. (2009) compared central ages with eU values for a larger set of Precambrian shield rocks and reported weaker or inconsistent trends, suggesting that variable Cl content rather than REA was controlling AFT annealing and age dispersion. These contrasting results are not surprising given the methods that were used. Central ages minimize the effect of age dispersion and therefore are not the best parameter for discerning REA effects, particularly for the samples of this study that exhibit "open jaw" radial plots (O'Sullivan and Parrish, 1995; fig. 3) that are a common feature of multi-kinetic AFT samples (Issler et al., 2005; Powell et al., 2018b; Schneider and Issler, 2018). Furthermore, it can be difficult to infer compositional controls on AFT annealing using Cl content alone, when OH and various cations can have a significant effect on AFT annealing (Carlson et al., 1999; Barbarand et al., 2003). Combining samples of different apatite composition and/or with different thermal histories may obscure or weaken any possible relationship between AFT age and eU.

Unlike the previous studies that used the external detector method where typically up to 20 age grains are measured, we use larger sets of AFT single grain ages (up to 40 grains per sample; Table 1) obtained using the LA-ICP-MS method to investigate intra-sample age dispersion with respect to eU and annealing kinetic parameters derived from detailed elemental data. Samples with the largest number of measured grains (30-40) have the largest age dispersion (21-57%) whereas those with <30 grains have much lower dispersion (10-21%; fig. 3). Clearly it is necessary to measure a sufficient number of grains in order to sample as broad a range of eU values and AFT ages as possible. Although we also observe a 'weak' negative correlation between central age and eU (fig. 2), single grain ages spanning hundreds of millions of years, or over a billion years in some cases, show a well-defined relationship between increasing eU and younger AFT age (fig. 4). Our bedrock AFT samples generally have near end-member fluorapatite compositions based on measured Cl concentration. Some samples show a broader range in track retentivity when other kinetic parameters such as r_{mr0} (or equivalent effective Cl) and D_{par}, are used but there is no clear correlation between age and apatite composition (fig. 4).

Instead, the extreme variations in eU seem to offer the best explanation for the observed AFT age heterogeneity (clear correlation with age, fig. 4). The effect of eU on fission-track retentivity may have a discernible link to long residence at low temperatures in or below the partial annealing zone.

The interplay between eU and the other dominant kinetic parameter (i.e. Cl) becomes complex in some instances where Cl concentrations are comparatively variable or elevated, or there is relative enrichment of other cations such as Fe (fig. 5 and fig. 6). This is clearly demonstrated by a counterintuitive association between eU and effective Cl (or inverse correlation with r_{mr0}, fig. 6). The Baffin Island semipelite sample 09SRB-M100 demonstrates a spurious correlation between eU and effective Cl/r_{mr0}, which implies there is a confounding variable or other kinetic parameter controlling retentivity. This is counter to the argument that high Cl and low r_{mr0} would signify higher retentivity, and high eU should hypothetically lower retentivity if greater damage is a proxy for enhanced annealing. An appropriate filter for samples is examining the AFT age-eU relationship. If a sample shows that effective Cl is heterogeneous in 'age-eU space' with a clear negative curvilinear age-eU correlation then eU is primarily driving retentivity, see Southampton Island and Superior Province samples. If clear effective Cl 'domains' or divisions are apparent when viewing age-eU relationships (sample 09SRBM100), this suggests Cl or another cation-site element is playing a greater role in controlling retentivity. Samples with more homogenous chemical compositions and low Cl show no such relationship between eU and effective Cl/r_{mr0} and denote eU as the primary driver of intra-sample age dispersion, which is reflected in plots of eU versus age that show age scatter across the entire range of Cl. There is likely some threshold where Cl begins to counteract the effects of REA or dominates fission-track retention, however this seems variable between samples and conceivably has an association with thermal history.

5.2 Elemental substitutions and compositional variation

The formula for apatite when considering substitutions (Barbarand et al., 2003) can be written as $X_{10}YO_4Z_2$ where, X = mainly Ca, Y = P, and Z = F, Cl, or OH. The most common substitutions on the X site are Fe^{2+}, Mn^{2+}, Na^{+}, REE^{3+} Sr^{2+} and U^{4+}, whereas Si and S occur on the Y site. The trivalent (REE^{3+}) cations substitute in pairs to maintain charge balance: $REE^{3+} + Si^{4+}$ proceeds to $Ca^{2+} + P^{5+}$ and $REE^{3+} + Na^{+}$ to $2Ca^{2+}$ (Barbarand et al., 2003 and refs. therein). We present two

examples where we try to further investigate the compositional controls on AFT grain ages from samples with high and low age dispersion. Sample PBA-98-743 from the Superior Province and 12NK-L18A3 from the northeast Slave craton are characterized by 36% and 14% dispersion, respectively (fig. 3). PBA-98-743 exhibits strong eU control on age (figs. 4 and 6), however 12NK-L18A3 does not (fig. 4). Moreover, the Slave sample is characterized by old ages despite high eU (high α-damage; see fig. 9), suggesting another kinetic control on retentivity.

Linear correlation matrices were performed on the elemental data (wt. %) for these two samples to assess the dominant interactions between the typical, known controls on retentivity (fig. 7). The data were standardized first to reduce any extreme variance between elements. Correlation coefficients associated with positive correlations are shown in black and variables that are anti-correlated are in white with the size of the circle corresponding to larger or smaller correlation coefficients (fig. 7A). For the Superior Province sample all linear correlations are shown in fig. 7A, however to assess the robustness of the relationship, only those that correspond to p-values of ≤0.01 or pass at 99% confidence level were retained (fig. 7B). F and Cl are anti-correlated as expected and in this case eU is most highly correlated with Ce (r = 0.677), La (r = 0.559), Cl (r = 0.490), Y (r = 0.456), Mn (r = 0.446) and is anti-correlated with F (r = -0.440). La and Ce are the most-highly correlated elements (r = 0.903). However, caution is advised in interpreting these relationships because in some cases many of the grains contain low or negligible elements but only a few grains are enriched and produce a statistically robust correlation (fig. 7C), as is the case with eU and La/Ce.

Figure 7D is a case where no clear age-eU relationship is observed and this is revealed in the correlation matrix (p-values of ≤0.01) as eU is not robustly correlated with any other element. The Slave craton sample is preferentially incorporating REE, Mn, Fe, Na, and Cl. The most highly correlated elements are La-Ce (r = 0.940), Mn-Y (r = 0.830), Mn-Fe (r = 0.777), Fe-Y (r = 0.748), Na-Mg (r = 0.723), Na-Cl (r = 0.715), and S-Cl (r = 0.597). These associations do not necessarily yield direct insight into retentivity (AFT age) but they do indicate the elements that are being incorporated into apatite grains from a particular bedrock sample, which may ultimately and indirectly aid in assessment of age dispersion. It is extremely important to point out that while many of these elements are highly correlated with one another, eU is the only element that exhibits a very consistent and strong (curvi)-linear relationship with AFT single-

grain ages in virtually all of our samples. This observation implies that α-radiation is a governing factor for AFT data from slowly-cooled settings.

5.3 Considering α-recoil and fission track damage accumulation

The majority of radiation damage results from α-recoil in the apatite lattice, whereas fission offers a minor damage contribution (for every 2 million ^{238}U nuclei undergoing α-decay only one fission event occurs; e.g. Donelick et al., 2005). The α-damage present in apatite will increase with time as a function of the parent nuclide content, but will also decrease with heating (Shuster and Farley, 2009). The mere presence of negative age-eU trends in our dataset (not commonly observed for apatite data), imply long residence at low temperatures below those required for annealing (or significant He retention), as this would not develop in old rocks where damage accumulation creates differences in retentivity. Our data empirically support the persistence of α-recoil damage over extremely long timescales in the AFT system (figs. 8 and 9) and that α-damage is characterized by slower annealing rates or different annealing kinetics than fission-track damage, as previously suggested (Fox and Shuster, 2014; Ritter and Märk, 1986; Willet et al., 2017).

An example of the relationship between α-damage and cooling age is shown in figure 8 where AFT and AHe data from the same location (Pinet et al., 2016) are plotted against eU and transposed into α-dose. Alpha dose is calculated following equation 5 of Nasdala et al. (2005) and is expressed as α/g.

$$D_\alpha = 8 \cdot \frac{C_U \cdot N_A \cdot 0.9928}{M_{238} \cdot 10^6} \cdot \left(e^{\lambda 238 t} - 1\right) + 7 \cdot \frac{C_U \cdot N_A \cdot 0.0072}{M_{235} \cdot 10^6} \cdot \left(e^{\lambda 235 t} - 1\right) + 6 \cdot \frac{C_{Th} \cdot N_A}{M_{232} \cdot 10^6} \cdot \left(e^{\lambda 232 t} - 1\right) \quad (1)$$

Where, C_U and C_{Th} are the actinide concentrations in ppm, N_A is Avogadro's number, and M_{238} (etc.) are the molecular weights of the parent isotopes, and λ_{238}, λ_{235}, λ_{232} are the decay constants for each. The *t* in the equation refers to the integration or accumulation time for α-particle self-irradiation. Traditionally, for zircon this time is taken as the time since crystallization and is presumably a reasonable assumption, however this becomes more difficult to assess for other minerals such as apatite that are more prone to greater damage annealing at moderate temperatures of <200°C.

The most difficult assumption regarding α-dose estimation is the integration time for self-irradiation, and here we refer to the integration time as the "effective dose accumulation time"

(t_{EDA}). We estimate the t_{EDA} for AFT as the mean of the 2σ minimum apatite U-Pb age for the sample, and when applicable, for AHe data the t_{EDA} is estimated by taking the difference between the oldest single-grain AFT age and the youngest single-grain AHe age, taken to be the last 'thermal event' experienced in the sample's history. The apatite U-Pb age estimate for AFT t_{EDA} seems to be a suitable approximation, however problems can arise in samples with low U that result in greater U-Pb age errors.

The apatite grains from Pinet et al. (2016) show a modest range in eU but interestingly the AFT data only capture the low eU and the AHe data have a greater spread in eU (fig. 8). This observation certainly suggests preferential selection of grains for each method, perhaps outside of the established routine of choosing pristine whole grains for (U-Th)/He analysis. The black dashed line is the ^{238}U α-damage percolation threshold of 1.9×10^{16} α/g from Ketcham et al., (2017) and is the point where diffusivity is expected to increase due to damage connectivity creating fast-path diffusion. These data clearly demonstrate the increase in AHe age going from low eU/low α-dose and increasing in age until the percolation threshold is reached whereby a decrease in age follows (this is very similar to the observed behaviour for zircon U-Th/He data (Guenthner et al., 2013). The AFT ages are pushed to the right of the damage threshold due to longer t_{EDA}, which dominates any effects of high or variable eU between single grains. When examining samples, the difference in t_{EDA} can explain why very different U and Th amounts between samples can result in similar overall age-eU trends. Visually the data display remarkable adherence to the α-dose threshold, despite the large difference in t_{EDA} between the AFT and AHe data. The AFT data are mostly to the right of the U percolation threshold even though those grains have low eU, whereas the AHe ages still show an increase and decrease in age (diffusivity) because the t_{EDA} is ~2.5x less than the AFT data. Furthermore, the eU variation has not been dampened by time, and longer t_{EDA} moves these grains into high damage at doses between 5×10^{16} to $>1 \times 10^{17}$ α/g.

Our α-dose plots imply that at least some fission tracks are impacted by α-recoil tracks. At this time it is not entirely clear why AFT ages behave similarly to AHe ages with respect to the recoil damage percolation threshold, however it may be due to their shared dependence on diffusive mechanisms that affect track annealing and ^{4}He retentivity. We envision difficulty in trying to develop a model to jointly explain these damage types, as the dimensions, frequencies, and

timescales (t_{EDA}) are very different. Now we examine our Canadian Shield AFT data with respect to the ^{238}U percolation threshold and discuss these relationships.

Figure 9 shows AFT data from the Canadian Shield selected from table 1. All AFT samples with long (and similar) t_{EDA} >1 Ga plot to the right of the damage threshold, whereas Grenvillian basement samples 02NKL-871 and P1420 from Powell et al. (2018a) with shorter t_{EDA} <1 Ga show an increase and subsequent decrease in AFT ages before and after the damage threshold, respectively. To better understand the damage relation with AFT age, it is notable that a very high eU sample (12NK-L18A3) displays high damage and high eU variance (σ^2) between single grains resulting in a relatively low spread in single-grain ages but moderate spread in damage level. There is no clear age-eU relationship for this sample. Conversely, sample 13LVA04 has very low eU (and low σ^2) and plots on the percolation threshold resulting in extreme age variability. High age scatter is expected for samples exhibiting high eU variability and especially for those near the percolation threshold – as this would be the region of greatest sensitivity to subtle changes in crystal damage and therefore changes in track annealing.

5.3 Implications for the apatite fission track and (U-Th)/He thermochronometers

In situ transmission electron microscopy performed on apatite has demonstrated non-thermal annealing of α-recoil damage and recovery of crystalline structure from fully-amorphous (pre-damaged) Durango apatite specimens through irradiation (Li et al., 2017). Damage recovery through α-healing has also been recently demonstrated for monazite, suggesting that natural monazite, like apatite (Ouchani et al., 1997), never becomes amorphous due to the effects of α-recoil (Seydoux-Guillaume et al., 2018). We do not believe that α-particles necessarily anneal fission tracks, as posited by Hendriks and Redfield (2005), but rather that α-recoil acts to destabilize fission tracks and therefore affects annealing rates. The process or mechanism by which α-recoil damage destabilizes fission tracks is not fully understood. However, some potential hypotheses are that (1) α-recoil interferes with existing fission-tracks directly, which in turn yields an easier-to-anneal track configuration, or that (2) α-damage disrupts the crystal lattice (as fission tracks are also lattice defects) making a partially altered lattice easier to mend than a pristine crystalline structure.

In addition to direct effects on damage annealing, it has also been suggested that preferential U and Th substitution in fluorapatite or chlorapatite causes a change in volume (decrease and

increase, respectively) of the apatite Ca (I) and Ca (II) polyhedron (Luo et al., 2009). This results in an increase in size and distortion of the Ca (II) site, allowing for preferential substitution of U and Th at both Ca sites in chlorapatite. This is an interesting observation because the Carlson et al., (1999) dataset documents that substitutions for Ca tend to reduce annealing rates in apatite but may also depend on a complex relationship with mixing at the halogen site (i.e. F/Cl/OH). The results of Luo et al., (2009) demonstrate that U and Th are structurally preferred in chlorapatite, so it is no surprise that previous work attributed differences in AFT ages to Cl rather than eU, as Cl is a dominant control on track retentivity. Our correlation matrices (fig. 7) also imply that fluorapatite is characterized by lower Cl and U-Th affinity, whereas chlorapatite shows a positive correlation between Cl and eU.

Enhanced annealing may be a purely structural effect from lattice distortions or convolved with the fact that in some cases those substitutions happen to be high α-emitters, thus introducing the likelihood for the degradation of fission track integrity that is most evident when thermal annealing is a secondary concern. It is not clear how other Ca-site substituting elements such as Fe that increase retentivity, would play a role in counteracting this effect and would obviously only do so if present in sufficient quantity within the lattice. A corollary exists in zircon where greater U and Th content increases microstructural deformation as further development and creep of lattice dislocations cause enhanced diffusivity of these elements (Timms et al., 2006). Increasing levels of grain deformation also seem to complicate ^{4}He diffusion in apatite by increasing retentivity through vacancies (Gerin et al., 2017) and dislocations acting as diffusive traps (McDannell et al., 2018).

Crystal lattice defects related to α-recoil might be a primary contributor to fission track instability. This could either be directly, or by association with substituting α-emitting parent nuclides such as U and Th. Interference between lattice defects due to α-recoil and fission-track defects could invariably result in α-recoil causing sufficient damage/healing to facilitate annealing, especially given the rarity of fission tracks with respect to α-recoil tracks. These effects could presumably overwhelm apatite fission tracks from rocks with variable U and Th concentrations that have been residing at lukewarm, near-surface conditions for hundreds of millions of years. In other cases involving more complex shallow burial and exhumation events, some amount of α-damage may be preserved for up to a billion years or more and never fully

annealed. In these scenarios, thermal annealing is mostly insignificant at <60°C, but α-induced damage could cumulatively modify the apatite lattice in proportion to the U and Th, thereby making fission tracks unstable and driving differential annealing at low temperatures – thereby yielding large AFT single-grain age dispersion. This is likely amplified by longer damage accumulation times and is more noticeable in samples with a range of eU. Fission tracks and α-damage both undergo annealing via diffusion processes (Ritter and Märk, 1986), which are regulated by crystallographic damage level; therefore they should be viewed and treated as a damage continuum with different timescale and kinetic dependencies.

5.3 Recommendations and questions for future work

The effects of REA on AFT ages in slowly-cooled settings is a complex problem that requires sufficient data to be able to evaluate relationships between chemical composition and age. Some factors to consider in future work to assist in addressing REA include:

1. Acquire enough age grains (>20) to capture and to characterise intra-sample AFT age dispersion.
2. Collect detailed elemental data for every sample including length and age grains; e.g. measured Cl is insufficient and could give misleading results.
3. Acquire apatite U-Pb age data to estimate t_{EDA}.
4. The choice of r_{mr0} equation is important and further work is needed to refine the relationship at high and low retentivity where existing models do not sufficiently capture variability in retentivity. This becomes especially important if bedrock samples are to be treated as multi-kinetic for thermal history modeling.

6. Conclusions

Apatites from bedrock samples across many areas of the Canadian Shield show coincident high single-grain age dispersion and variable eU. There are no other clear intra-sample, compositional controls such as Cl, Fe, or REE substitution that demonstrate a strong relation with AFT age. In some isolated cases there are some grains enriched in elements known to enhance fission-track retentivity, however these are typically only a few grains from within a sample. Our dataset further establishes the necessity of acquiring compositional data for interpreting apatite fission-track analyses, especially in slowly-cooled settings. Our AFT data strongly support the notion

that REA by α-recoil is related to the eU content within apatite. Complications arise between co-existing, specific elemental substitutions that independently act to either enhance or reduce fission track annealing. The exact mechanism for enhanced annealing is likely multifaceted but may be due to α-damage affecting tracks directly, α-damage and elemental substitutions causing lattice defects that promote track instability, α-damage self-healing reducing lattice damage and shortening tracks, or a combination of these effects that are exacerbated in settings where thermal annealing is minimal and timescales for α-damage accumulation are long.

Acknowledgements

We thank R. Ketcham for discussions on topics presented in this paper and J. Powell for internal review of the manuscript. This work was funded by the Geomapping for Energy and Minerals Program (Trans-GEM) through Natural Resources Canada, Land and Minerals Sector, Geological Survey of Canada. NRCan contribution number 2018XXXX. Correlation matrix analyses performed using RStudio v. 1.1.453 (R Core Team, 2018) using the corrplot and cor.mtest packages (Wei and Simko, 2017). Other figures made using Generic Mapping Tools (GMT) v. 5.4 (Wessel et al., 2013).

References

Ault, A.K., Flowers, R.M. and Bowring, S.A. (2009) Phanerozoic burial and unroofing history of the western Slave craton and Wopmay orogen from apatite (U–Th)/He thermochronometry. Earth and Planetary Science Letters 284, 1-11.

Barbarand, J., Carter, A., Wood, I. and Hurford, T. (2003) Compositional and structural control of fission-track annealing in apatite. Chemical Geology 198, 107-137.

Baughman, J.S., Flowers, R.M., Metcalf, J.R. and Dhansay, T. (2017) Influence of radiation damage on titanite He diffusion kinetics. Geochimica et Cosmochimica Acta 205, 50-64.

Berman, R., Sanborn-Barrie, M., Rayner, N. and Whalen, J. (2013) The tectonometamorphic evolution of Southampton Island, Nunavut: Insight from petrologic modeling and in situ SHRIMP geochronology of multiple episodes of monazite growth. Precambrian Research 232, 140-166.

Berman, R.G., Davis, W.J., Corrigan, D. and Nadeau, L. (2015) Insights into the tectonothermal history of Melville Peninsula, Nunavut, provided by in situ SHRIMP geochronology and thermobarometry. Geological Survey of Canada, Current Research, p. 22.

Bleeker, W., Ketchum, J.W. and Davis, W. (1999) The Central Slave Basement Complex, Part II: age and tectonic significance of high-strain zones along the basement-cover contact. Canadian Journal of Earth Sciences 36, 1111-1130.

Burgess, P.M. (2008) Phanerozoic evolution of the sedimentary cover of the North American craton. Sedimentary basins of the world 5, 31-63.
Cairns, S., Relf, C., MacLachlan, K. and Davis, W. (2005) Neoarchean decoupling of upper-and mid-crustal tectonothermal domains in the southeast Slave Province: evidence from the Walmsley Lake area. Canadian Journal of Earth Sciences 42, 869-894.
Carlson, W.D. (1990) Mechanisms and kinetics of apatite fission-track annealing. American Mineralogist;(United States) 75.
Carlson, W.D., Donelick, R.A. and Ketcham, R.A. (1999) Variability of apatite fission-track annealing kinetics: I. Experimental results. American mineralogist 84, 1213-1223.
Carpena, J. and Lacout, J.-L. (2010) Thermal annealing of fission tracks in synthetic apatites. Nuclear Instruments and Methods in Physics Research Section B: Beam Interactions with Materials and Atoms 268, 3191-3194.
Carter, A. (1990) The thermal history and annealing effects in zircons from the Ordovician of North Wales. International Journal of Radiation Applications and Instrumentation. Part D. Nuclear Tracks and Radiation Measurements 17, 309-313.
Chakoumakos, B.C., Murakami, T., Lumpkin, G.R. and Ewing, R.C. (1987) Alpha-decay-induced fracturing in zircon: The transition from the crystalline to the metamict state. Science 236, 1556-1559.
Chew, D.M. and Donelick, R.A. (2012) Combined apatite fission track and U-Pb dating by LA-ICP-MS and its application in apatite provenance analysis. Quantitative mineralogy and microanalysis of sediments and sedimentary rocks: Mineralogical Association of Canada Short Course 42, 219-247.
Cookenboo, H.O., Orchard, M.J. and Daoud, D.K. (1998) Remnants of Paleozoic cover on the Archean Canadian Shield: limestone xenoliths from kimberlite in the central Slave craton. Geology 26, 391-394.
Corrigan, D., Nadeau, L., Brouillette, P., Wodicka, N., Houle, M.G., Tremblay, T., Machado, G. and Keating, P. (2013) Overview of the GEM Multiple Metals - Melville Peninsula project, central Melville Peninsula, Nunavut. Geological Survey of Canada, p. 17.
Davis, W.J., Berman, R.G., Nadeau, L. and Percival, J.A. (2014) U-Pb Zircon Geochronology of a transect across the Thelon Tectonic Zone, Queen Maud region, and adjacent Rae craton, Kitikmeot region, Nunavut, Canada, Open File 7652. Geological Survey of Canada, pp. 1-39.
Djimbi, D.M., Gautheron, C., Roques, J., Tassan-Got, L., Gerin, C. and Simoni, E. (2015) Impact of apatite chemical composition on (U-Th)/He thermochronometry: An atomistic point of view. Geochimica et Cosmochimica Acta 167, 162-176.
Donelick, R.A., Ketcham, R.A. and Carlson, W.D. (1999) Variability of apatite fission-track annealing kinetics: II. Crystallographic orientation effects. American mineralogist 84, 1224-1234.
Donelick, R.A., O'Sullivan, P.B. and Ketcham, R.A. (2005) Apatite fission-track analysis. Reviews in Mineralogy and Geochemistry 58, 49-94.
Farley, K.A., Wolf, R.A. and Silver, L.T. (1996) The effects of long alpha-stopping distances on (U-Th)/He ages. Geochimica et Cosmochimica Acta 60, 4223-4229.
Feinstein, S., Kohn, B., Osadetz, K., Everitt, R. and O'Sullivan, P. (2009) Variable Phanerozoic thermal history in the Southern Canadian Shield: Evidence from an apatite fission track profile at the Underground Research Laboratory (URL), Manitoba. Tectonophysics 475, 190-199.

Fitzgerald, P.G., Baldwin, S.L., Webb, L.E. and O'Sullivan, P.B. (2006) Interpretation of (U–Th)/He single grain ages from slowly cooled crustal terranes: A case study from the Transantarctic Mountains of southern Victoria Land. Chemical Geology 225, 91-120.

Flowers, R.M. (2009) Exploiting radiation damage control on apatite (U–Th)/He dates in cratonic regions. Earth and Planetary Science Letters 277, 148-155.

Flowers, R.M. and Kelley, S.A. (2011) Interpreting data dispersion and "inverted" dates in apatite (U–Th)/He and fission-track datasets: An example from the US midcontinent. Geochimica et Cosmochimica Acta 75, 5169-5186.

Flowers, R.M., Ketcham, R.A., Shuster, D.L. and Farley, K.A. (2009) Apatite (U–Th)/He thermochronometry using a radiation damage accumulation and annealing model. Geochimica et Cosmochimica Acta 73, 2347-2365.

Fox, M. and Shuster, D.L. (2014) The influence of burial heating on the (U–Th)/He system in apatite: Grand Canyon case study. Earth and Planetary Science Letters 397, 174-183.

Gautheron, C., Barbarand, J., Ketcham, R.A., Tassan-Got, L., van der Beek, P., Pagel, M., Pinna-Jamme, R., Couffignal, F. and Fialin, M. (2013) Chemical influence on α-recoil damage annealing in apatite: Implications for (U–Th)/He dating. Chemical Geology 351, 257-267.

Gautheron, C., Tassan-Got, L., Barbarand, J. and Pagel, M. (2009) Effect of alpha-damage annealing on apatite (U–Th)/He thermochronology. Chemical Geology 266, 157-170.

Gerin, C., Gautheron, C., Oliviero, E., Bachelet, C., Djimbi, D.M., Seydoux-Guillaume, A.-M., Tassan-Got, L., Sarda, P., Roques, J. and Garrido, F. (2017) Influence of vacancy damage on He diffusion in apatite, investigated at atomic to mineralogical scales. Geochimica et Cosmochimica Acta 197, 87-103.

Gleadow, A. and Duddy, I. (1981) A natural long-term track annealing experiment for apatite. Nuclear tracks 5, 169-174.

Green, P. (1988) The relationship between track shortening and fission track age reduction in apatite: combined influences of inherent instability, annealing anisotropy, length bias and system calibration. Earth and Planetary Science Letters 89, 335-352.

Green, P. and Duddy, I. (2006) Interpretation of apatite (U–Th)/He ages and fission track ages from cratons. Earth and Planetary Science Letters 244, 541-547.

Green, P., Duddy, I., Gleadow, A., Tingate, P. and Laslett, G. (1986) Thermal annealing of fission tracks in apatite: 1. A qualitative description. Chemical Geology: Isotope Geoscience section 59, 237-253.

Green, P., Duddy, I., Laslett, G., Hegarty, K., Gleadow, A.W. and Lovering, J. (1989) Thermal annealing of fission tracks in apatite 4. Quantitative modelling techniques and extension to geological timescales. Chemical Geology: Isotope Geoscience section 79, 155-182.

Green, P.F., Crowhurst, P.V., Duddy, I.R., Japsen, P. and Holford, S.P. (2006) Conflicting (U–Th)/He and fission track ages in apatite: enhanced He retention, not anomalous annealing behaviour. Earth and Planetary Science Letters 250, 407-427.

Guenthner, W.R., Reiners, P.W., Drake, H. and Tillberg, M. (2017) Zircon, titanite, and apatite (U-Th)/He ages and age-eU correlations from the Fennoscandian Shield, southern Sweden. Tectonics.

Guenthner, W.R., Reiners, P.W., Ketcham, R.A., Nasdala, L. and Giester, G. (2013) Helium diffusion in natural zircon: Radiation damage, anisotropy, and the interpretation of zircon (U-Th)/He thermochronology. American Journal of Science 313, 145-198.

Hasebe, N., Barbarand, J., Jarvis, K., Carter, A. and Hurford, A.J. (2004) Apatite fission-track chronometry using laser ablation ICP-MS. Chemical Geology 207, 135-145.
Hendriks, B. and Redfield, T. (2005) Apatite fission track and (U-Th)/He data from Fennoscandia: An example of underestimation of fission track annealing in apatite. Earth and Planetary Science Letters 236, 443-458.
Hendriks, B. and Redfield, T. (2006) Reply to: Comment on "Apatite Fission Track and (U–Th)/He data from Fennoscandia: An example of underestimation of fission track annealing in apatite" by BWH Hendriks and TF Redfield. Earth and Planetary Science Letters 248, 569-577.
Hoffman, P.F., Bally, A. and Palmer, A. (1989) Precambrian geology and tectonic history of North America. The geology of North America—an overview, 447-512.
Isachsen, C.E. and Bowring, S.A. (1994) Evolution of the Slave Craton. Geology 22, 917-920.
Issler, D., Grist, A. and Stasiuk, L. (2005) Post-Early Devonian thermal constraints on hydrocarbon source rock maturation in the Keele Tectonic Zone, Tulita area, NWT, Canada, from multi-kinetic apatite fission track thermochronology, vitrinite reflectance and shale compaction. Bulletin of Canadian Petroleum Geology 53, 405-431.
Kasuya, M. and Naeser, C.W. (1988) The effect of α-damage on fission-track annealing in zircon. International Journal of Radiation Applications and Instrumentation. Part D. Nuclear Tracks and Radiation Measurements 14, 477-480.
Ketcham, R.A. (2015) Calculation of stoichiometry from EMP data for apatite and other phases with mixing on monovalent anion sites. American mineralogist 100, 1620-1623.
Ketcham, R.A., Carter, A., Donelick, R.A., Barbarand, J. and Hurford, A.J. (2007) Improved measurement of fission-track annealing in apatite using c-axis projection. American mineralogist 92, 789-798.
Ketcham, R.A., Donelick, R.A. and Carlson, W.D. (1999) Variability of apatite fission-track annealing kinetics; III, Extrapolation to geological time scales. American mineralogist 84, 1235-1255.
Ketcham, R.A., Gautheron, C., Recanati, A. and Rahn, M. (2017) Possible influence of alpha recoil track percolation on helium diffusivity in apatite, Goldschmidt Abstracts. Geochemical Society, Paris, France, p. 1983.
Kohn, B.P., Gleadow, A.J., Brown, R.W., Gallagher, K., Lorencak, M. and Noble, W.P. (2005) Visualizing thermotectonic and denudation histories using apatite fission track thermochronology, in: Reiners, P.W., Ehlers, T.A. (Eds.), Reviews in Mineralogy and Geochemistry. Mineralogical Society of America Geochemical Society, Chantilly, Virginia, pp. 527-565.
Kohn, B.P., Lorencak, M., Gleadow, A.J., Kohlmann, F., Raza, A., Osadetz, K.G. and Sorjonen-Ward, P. (2009) A reappraisal of low-temperature thermochronology of the eastern Fennoscandia Shield and radiation-enhanced apatite fission-track annealing. Geological Society, London, Special Publications 324, 193-216.
Larson, S.Å., Cederbom, C.E., Tullborg, E.-L. and Stiberg, J.-P. (2006) Comment on "Apatite fission track and (U–Th)/He data from Fennoscandia: An example of underestimation of fission track annealing in apatite" by Hendriks and Redfield [Earth Planet. Sci. Lett. 236 (443–458)]. Earth and Planetary Science Letters 248, 561-568.
Lavoie, D., Pinet, N., Dietrich, J., Zhang, S., Hu, K., Asselin, E., Chen, Z., Bertrand, R., Galloway, J. and Decker, V. (2013) Geological framework, basin evolution, hydrocarbon

system data and conceptual hydrocarbon plays for the Hudson Bay and Foxe basins, Canadian Arctic. Geological Survey of Canada, Open File Report 7363, 213.
Li, W., Shen, Y., Zhou, Y., Nan, S., Chen, C.-H. and Ewing, R.C. (2017) In situ TEM observation of alpha-particle induced annealing of radiation damage in Durango apatite. Scientific reports 7, 14108.
Lumpkin, G.R., Eby, R.K. and Ewing, R.C. (1991) Alpha-recoil damage in titanite (CaTiSiO 5): Direct observation and annealing study using high resolution transmission electron microscopy. Journal of Materials Research 6, 560-564.
Luo, Y., Hughes, J.M., Rakavan, J. and Pan, Y. (2009) Site preference of U and Th in Cl, F, and Sr apatites. American mineralogist 94, 345-351.
McCracken, A.D., Armstrong, D.K. and Bolton, T.E. (2000) Conodonts and corals in kimberlite xenoliths confirm a Devonian seaway in central Ontario and Quebec. Canadian Journal of Earth Sciences 37, 1651-1663.
McDannell, K.T., Zeitler, P.K., Janes, D.G., Idleman, B.D. and Fayon, A.K. (2018) Screening apatites for (U-Th)/He thermochronometry via continuous ramped heating: He age components and implications for age dispersion. Geochimica et Cosmochimica Acta 223, 90-106.
McKeon, R.E. (2012) Apatite U-Th/He Thermochronometry in Slowly Eroding Landscapes: Addressing Age Dispersion to Understand Appalachian Topographic Development, Earth and Environmental Sciences. Lehigh University.
Miall, A.D. and Blakey, R.C. (2008) The Phanerozoic tectonic and sedimentary evolution of North America. Sedimentary basins of the world 5, 1-29.
Murakami, T., Chakoumakos, B.C., Ewing, R.C., Lumpkin, G.R. and Weber, W.J. (1991) Alpha-decay event damage in zircon. American mineralogist 76, l5l0-1532.
Nadzri, A., Schauries, D., Mota-Santiago, P., Trautmann, C., Gleadow, A.J.W., Hawley, A. and Kluth, P. (2017) Composition and orientation dependent annealing of ion tracks in apatite - Implications for fission track thermochronology. Chemical Geology 451, 9-16.
Naeser, C. and Faul, H. (1969) Fission track annealing in apatite and sphene. Journal of Geophysical Research 74, 705-710.
Nasdala, L., Hanchar, J.M., Kronz, A. and Whitehouse, M.J. (2005) Long-term stability of alpha particle damage in natural zircon. Chemical Geology 220, 83-103.
Nasdala, L., Wenzel, M., Vavra, G., Irmer, G., Wenzel, T. and Kober, B. (2001) Metamictisation of natural zircon: accumulation versus thermal annealing of radioactivity-induced damage. Contrib. Miner. Petrol. 141, 125-144.
Nassichuk, W. and McIntyre, D. (1995) Cretaceous and Tertiary fossils discovered in kimberlites at Lac de Gras in the Slave Province, Northwest Territories. Geological Survey of Canada Current Research 1995, 109-114.
O'Sullivan, P.B. and Parrish, R.R. (1995) The importance of apatite composition and single-grain ages when interpreting fission track data from plutonic rocks: a case study from the Coast Ranges, British Columbia. Earth and Planetary Science Letters 132, 213-224.
Ouchani, S., Dran, J.-C. and Chaumont, J. (1997) Evidence of ionization annealing upon helium-ion irradiation of pre-damaged fluorapatite. Nuclear Instruments and Methods in Physics Research Section B: Beam Interactions with Materials and Atoms 132, 447-451.
Partin, C., Bekker, A., Corrigan, D., Modeland, S., Francis, D. and Davis, D. (2014) Sedimentological and geochemical basin analysis of the Paleoproterozoic Penrhyn and Piling groups of Arctic Canada. Precambrian Research 251, 80-101.

Percival, J., McNicoll, V., Brown, J. and Whalen, J. (2004) Convergent margin tectonics, central Wabigoon subprovince, Superior Province, Canada. Precambrian Research 132, 213-244.
Percival, J., Skulski, T., Sanborn-Barrie, M., Stott, G., Leclair, A., Corkery, M. and Boily, M. (2012) Geology and tectonic evolution of the Superior Province, Canada. Tectonic Styles in Canada: The Lithoprobe Perspective. Geol Assoc Canada Spec Paper 49, 321-378.
Pinet, N., Kohn, B. and Lavoie, D. (2016) The ups and downs of the Canadian Shield: 1-preliminary results of apatite fission track analysis from Hudson Bay region. Geological Survey of Canada, p. 59.
Pinet, N., Lavoie, D., Dietrich, J., Hu, K. and Keating, P. (2013) Architecture and subsidence history of the intracratonic Hudson Bay Basin, northern Canada. Earth-Science Reviews 125, 1-23.
Powell, J., Schneider, D.A., Desrochers, A., Flowers, R.M., Metcalf, J., Gaidies, F. and Stockli, D.F. (2018a) Low-temperature thermochronology of Anticosti Island: a case study on the application of conodont (U-Th)/He thermochronology to carbonate basin analysis. Marine and Petroleum Geology.
Powell, J.W., Schneider, D.A. and Issler, D.R. (2018b) Application of multi-kinetic apatite fission track and (U-Th)/He thermochronology to source rock thermal history: a case study from the Mackenzie Plain, NWT, Canada. Basin Research 30, 497-512.
Price, P. and Walker, R. (1963) Fossil tracks of charged particles in mica and the age of minerals. Journal of Geophysical Research 68, 4847-4862.
R Core Team (2018) R: A language and environment for statistical computing. R Foundation for Statistical Computing, Vienna, Austria. URL https://www.R-project.org/.
Rayner, N., Chakungal, J. and Sanborn-Barrie, M. (2011) New U-Pb geochronological results from plutonic and sedimentary rocks of Southampton Island, Nunavut. Geological Survey of Canada.
Recanati, A., Gautheron, C., Barbarand, J., Missenard, Y., Pinna-Jamme, R., Tassan-Got, L., Carter, A., Douville, É., Bordier, L. and Pagel, M. (2017) Helium trapping in apatite damage: Insights from (U-Th-Sm)/He dating of different granitoid lithologies. Chemical Geology 470, 116-131.
Ritter, W. and Märk, T. (1986) Radiation damage and its annealing in apatite. Nuclear Instruments and Methods in Physics Research Section B: Beam Interactions with Materials and Atoms 14, 314-322.
Schneider, D.A. and Issler, D.R. (2018) Application of low-temperature thermochronology to hydrocarbon exploration, in: Malusa, M.G., Fitzgerald, P. (Eds.), Fission-Track Thermochronology and its Application to Geology, 1 ed. Springer International Publishing, New York, p. 676.
Seiler, C., Gleadow, A. and Kohn, B. (2013) Apatite fission track dating by LA-ICP-MS and External Detector Method: How do they stack up?, AGU Fall Meeting abstracts.
Seydoux-Guillaume, A.-M., Deschanels, X., Baumier, C.d., Neumeier, S., Weber, W.J. and Peuget, S. (2018) Why natural monazite never becomes amorphous: experimental evidence for alpha self-healing. American mineralogist 10.2138./am-2018-6447.
Shuster, D.L. and Farley, K.A. (2009) The influence of artificial radiation damage and thermal annealing on helium diffusion kinetics in apatite. Geochimica et Cosmochimica Acta 73, 6183-6196.
Shuster, D.L., Flowers, R.M. and Farley, K.A. (2006) The influence of natural radiation damage on helium diffusion kinetics in apatite. Earth and Planetary Science Letters 249, 148-161.

Stasiuk, L.D., Sweet, A.R. and Issler, D.R. (2006) Reconstruction of burial history of eroded Mesozoic strata using kimberlite shale xenoliths, volcaniclastic and crater facies, Northwest Territories, Canada. International Journal of Coal Geology 65, 129-145.

Timms, N.E., Kinny, P.D. and Reddy, S.M. (2006) Enhanced diffusion of Uranium and Thorium linked to crystal plasticity in zircon. Geochemical Transactions 7, 1-16.

Vermeesch, P. (2012) On the visualisation of detrital age distributions. Chemical Geology 312, 190-194.

Vermeesch, P. (2017) Statistics for LA-ICP-MS based fission track dating. Chemical Geology 456, 19-27.

Wagner, G. (1968) Fission track dating of apatites. Earth and Planetary Science Letters 4, 411-415.

Weber, W., Ewing, R. and Meldrum, A. (1997) The kinetics of alpha-decay-induced amorphization in zircon and apatite containing weapons-grade plutonium or other actinides. Journal of nuclear materials 250, 147-155.

Wei, T. and Simko, V. (2017) R package "corrplot": Visualization of a Correlation Matrix (Version 0.84). Available from https://github.com/taiyun/corrplot.

Wessel, P., Smith, W.H., Scharroo, R., Luis, J. and Wobbe, F. (2013) Generic mapping tools: improved version released. Eos, Transactions American Geophysical Union 94, 409-410.

Whitmeyer, S.J. and Karlstrom, K.E. (2007) Tectonic model for the Proterozoic growth of North America. Geosphere 3, 220-259.

Willett, C.D., Fox, M. and Shuster, D.L. (2017) A helium-based model for the effects of radiation damage annealing on helium diffusion kinetics in apatite. Earth and Planetary Science Letters 477, 195-204.

Zeitler, P.K., Enkelmann, E., Thomas, J.B., Watson, E.B., Ancuta, L.D. and Idleman, B.D. (2017) Solubility and trapping of helium in apatite. Geochimica et Cosmochimica Acta 209, 1-8.

Zhang, S. and Pell, J. (2014) Conodonts recovered from the carbonate xenoliths in the kimberlites confirm the Paleozoic cover on the Hall Peninsula, Nunavut. Canadian Journal of Earth Sciences 51, 142-155.

FIGURE CAPTIONS

Figure 1. Map of the Canadian Shield with simplified geologic domains modified from Whitmeyer and Karlstrom (2007). Bedrock AFT samples are shown as circles with their corresponding central age, red points are LA-ICP-MS AFT samples and the orange point is the published Pinet et. al. (2016) sample. Areas in purple show Paleozoic succession of Hudson Bay, sub-basins, and surrounding Arctic platform, which imply bedrock has been at or near the present surface since (at least) the Ordovician. Refer to table 1 and text in section 4 for more information on AFT samples. Missing section in central Hudson Bay is younger overlying Mesozoic-Cenozoic sediment. Quebec Grenvillian and Cumberland Peninsula, Baffin Island samples are shown and discussed for comparison only, as they have a more complex thermal history compared to the Canadian Shield samples. THO = Trans-Hudson Orogen; GSL = Great Slave Lake shear zone; STZ = Snowbird Tectonic Zone; CP = Cumberland Peninsula; HP = Hall Peninsula; AB = Athabasca Basin; TB = Thelon Basin.

Figure 2. Conventional plot of eU content versus AFT age as well as mean track length for all bedrock samples. Other than the two high eU samples there is a decrease in age with eU. A simple linear regression (removing the highest two eU outliers) produces an R^2 value of 0.38. Highest eU grains clearly have the shortest MTL, however there are not enough intermediate-to-high eU data to confidently extrapolate the relationship.

Figure 3. Radial plots (log transformed) from DensityPlotter v. 8.2 for ICP-MS AFT data. Open jaw-type plots are typical of our dataset and are generally interpreted as meaning that multiple age populations are present – a common feature of detrital AFT datasets. Refer to table 1 for sample information. As an example of single-grain age dispersion effects, we have shown the two-component mixture model ages associated with age peaks of ca. 160 and ca. 75 Ma for sample 09SRB-M100. This illustrates how the central age for a sample can be misleading in cases of high dispersion. For sample 14SUB-H43A the opposite is true as this sample only has 10% age dispersion and lower *n*.

Figure 4. Bedrock sample AFT age versus eU and effective Cl for each sample in Table 1. Notice that each sample has a negative age-eU trend for single grains. There is no clear age relationship with effective Cl. Samples in color reference those in fig. 9.

Figure 5. Scatter plots of other Canadian Shield AFT examples. (A) An example from Pinet et al. (2016) showing the relationship between ^{238}U and age. The relation is similar to our data except not as well defined given that there are a low number of grains dated and eU was not calculated. (B) Sample 09SRB-M100C1 from Baffin Island shows a spurious relationship between AFT age and kinetic parameters eU and effective Cl/r_{mr0} (discussed in text, shown in fig. 6) that is not readily apparent when effective Cl is plotted against AFT age shown here. (C) Sample 14SUB-H43A also from Baffin Island displays lower eU variability than most samples and all single grains are in a range of "typical apatite" eU, it also has characteristic highly clustered effective Cl values suggesting low kinetic variability between grains. This relationship results in the "appearance" of less age variability, which may be naturally inherent to the sample or a result of unintended grain selection preference.

Figure 6. Examples of the relationship between eU and AFT age, effective Cl, and r_{mr0}. The Baffin Island sample exhibits behaviour indicative of Cl or another element controlling retentivity (> than any eU effect), whereas the other samples suggest eU is controlling retentivity. The last panels are normalized to show both samples PBA-98-743 and 03-GRS-013 together. Unfilled symbols are values outside the color ramp maximum. Trend lines (reduced major axis regression) are for visual purposes only, to highlight the spurious correlation (upper panel) and the lack of correlation (middle panel) between eU and effective Cl (or r_{mr0}).

Figure 7. Correlation matrices for standardized EPMA compositional analyses. Analyses are for Cl, eU, F, Fe, Mg, Mn, Na, S, Sr, and REE (Ce, La, Y) in wt. % shown in hierarchical clustering of correlation coefficients and (B and D) only show correlations with p-values <0.01 or at the 99% confidence level. Positive (+1, black) or negative (anti-) correlation (-1, white) is shown with the size of the corresponding circle equal to the linear correlation coefficient (i.e. small circle is low correlation coefficient and *vice versa*). Notice the anti-correlation between F and Cl as expected. (A, B) Examples are shown for the Superior Province sample PBA-98-743 that displays eU variability in relation with single-grain AFT age (fig. 3 and fig. 5) versus sample 12NK-L18A3 with very high eU (>>100 ppm) and no obvious age-eU relationship (D). Note that care is required during interpretation of these relationships, as some grains may seem highly correlated but are represented by only a few EPMA analyses/grains, where the majority of grains are zero/below detection limit, which is typically the case for REE, seen in panel C plots of normalized eU, Ce, and La for sample PBA-98-743. Best-fit linear trend (black line) and correlation coefficient (r) are shown for each plot (C).

Figure 8. Example of both AFT and AHe data from Melville Peninsula with respect to α-dose from Pinet et al., (2016). **(A)** AFT (sample 09SZ-23-01; circles) and AHe ages (samples 09SZ23-01 and 09SZ24-01; hexagons) with respect to eU. The measured ^{238}U value is used as a proxy for eU here. This is a good approximation because most accompanying AHe single grains have low Th, <10 ppm. **(B)** AFT and AHe ages plotted against the estimated α-dose. The AFT data are older vintage without U-Pb ages; therefore we used the t_{EDA} from nearby AFT sample 10CXAD-086.

Figure 9. Plot of estimated α-dose vs. age for selected Canadian Shield AFT samples summarized in table 1 and shown on fig. 1. Samples with long t_{EDA} plot at high damage levels above the threshold and show negative age-α-dose correlations, whereas samples with shorter t_{EDA} show the expected positive relationship at low damage below the percolation threshold. Collectively these samples capture the full range in α-dose or damage level. 13LVA04 and 12NKL18A3 demonstrate the effect of low/high eU variance on α-dose. Black dashed line is the percolation threshold from Ketcham et al., (2017). Single-grain age errors not shown for clarity.

Table 1. Summary of apatite fission track results from across the Canadian Shield (see fig. 1 for locations). All age data were obtained by LA-ICP-MS analysis. All of our samples fail the chi-squared test. Percent difference between the central and pooled age is shown. Single-grain age span between the oldest/youngest grains (not including error) shows the AFT heterogeneity within samples and eU range is given with the mean eU in brackets. Sample 03-GRS-013 has a single anomalously old grain, which refers to the age span value in brackets. Refer to text for discussion of results. Note: some single grains within samples were unable to be probed or do not have chemical data, therefore an effective Cl/r_{mr0} value was unable to be calculated for those grains, in these instances the average respective kinetic parameter value for the entire dataset was used for plotting purposes. See supplementary material for full AFT dataset.

Table 1. *Apatite fission track results for the Canadian Shield*

Sample	GSC Lab #	Rock Type	Long. DD	Lat. DD	no. age gr.	grain age span (My)	Pooled Age (Ma)	1σ (Ma)	Central Age (Ma)	1σ (Ma)	% diff	MTL (µm)	1σ (µm)	track count	avg. D_{par} (µm)	avg. eU (ppm)	avg. r_{mr0}	avg. Cl (apfu)	Eff. Cl (apfu)	U-Pb age pop. (Ma)	2σ (Ma)
Western Superior Province, Ontario																					
PBA-98-743	5479	tonalite	-90.12120	49.92996	40	1233	572	16	597	37	4	12.07	1.94	130	1.89	1-19 [7]	0.84	0.008	0.002	2971	174
03-GRS-013	8105	tonalite qtz. diorite	-87.89872	53.66566	40	715 [2119]	414	14	447	34	8	12.51	1.63	131	1.91	1-241 [33]	0.84	0.003	-0.005	3009	94
Slave Province, Northwest Territories																					
BNB97-035	8460	biotite granitoid	-112.9215	63.23258	40	495	229	22	272	16	17	12.75	1.80	116	1.72	0.2-98 [21]	0.85	0.006	-0.041	2858	124
12-DRA03-001	8313	plag. porph. intrusive	-114.8500	63.33333	40	378	336	11	344	14	2	12.04	2.39	131	1.87	2-55 [16]	0.83	0.019	0.023	2628	96
12NK-L18A3	10889	granitic gneiss	-102.0765	66.14816	26	236	392	9	397	13	1	11.91	2.06	78	1.85	139-655 [339]	0.79	0.012	0.135	1788	40
Churchill-Rae Province, Melville Peninsula, Nunavut																					
SNB-01-M2055	7271	foliated tonalite	-91.11273	66.87706	30	482	349	10	356	18	2	12.19	2.30	130	2.00	0.2-46 [14]	0.84	0.003	0.002	1940	68
10CXAD-086A	10313	gabbro-anorthosite	-82.05779	67.82549	40	1832	363	28	460	44	24	12.60	1.79	132	2.12	0.2-73 [13]	0.82	0.029	0.059	1803	73
13LVA04	11068	gabbro	-101.7240	62.69358	40	739	546	34	557	31	2	12.44	2.06	121	1.92	3-42 [7]	0.80	0.012	0.097	2224	125
09SZ-23-01*	-	granitic gneiss	-82.84220	69.49660	19	406	463	30	486	27	5	12.18	1.58	100	1.67	11-20 [14]**	0.85	0.016	-0.043	-	-
Churchill-Rae Province, Southampton Island, Nunavut																					
07CYA-M38B	9422	gabbroic anorthosite	-83.60701	64.84525	40	595	342	10	384	21	12	12.22	2.00	132	1.90	1-71 [22]	0.84	0.024	0.007	1834	60
07CYA-M133A	9558	diorite	-81.90056	64.54453	15	357	364	11	375	17	3	11.57	2.16	101	2.26	7-258 [74]	0.80	0.086	0.098	1812	79
Rae craton, southern Baffin Island, Nunavut																					
09SRB-M100	10840	semipelite	-64.48663	65.46074	35	222	97	4	102	8	5	12.94	2.23	41	2.14	1-69 [22]	0.83	0.023	0.041	1674	35
14SUB-H43A	11261	gt-bt psammite	-66.91792	64.56119	25	256	440	11	442	12	0.5	12.46	1.72	130	2.29	16-35 [26]	0.82	0.022	0.045	1782	38
Grenville Province, Quebec																					
02NKL-871	7626	granitic orthogneiss	-62.64094	50.26647	35	540	161	5	177	13	9	12.27	1.80	135	1.83	2-160 [31]	0.85	0.008	-0.018	951	38

*Sample from Pinet et al. (2016)

**Calculated by uniformly applying associated single-grain (U-Th)/He average Th and Sm concentrations with each AFT ^{238}U measurement to give a more representative value for the eU content.

Figure1

Click here to download high resolution image

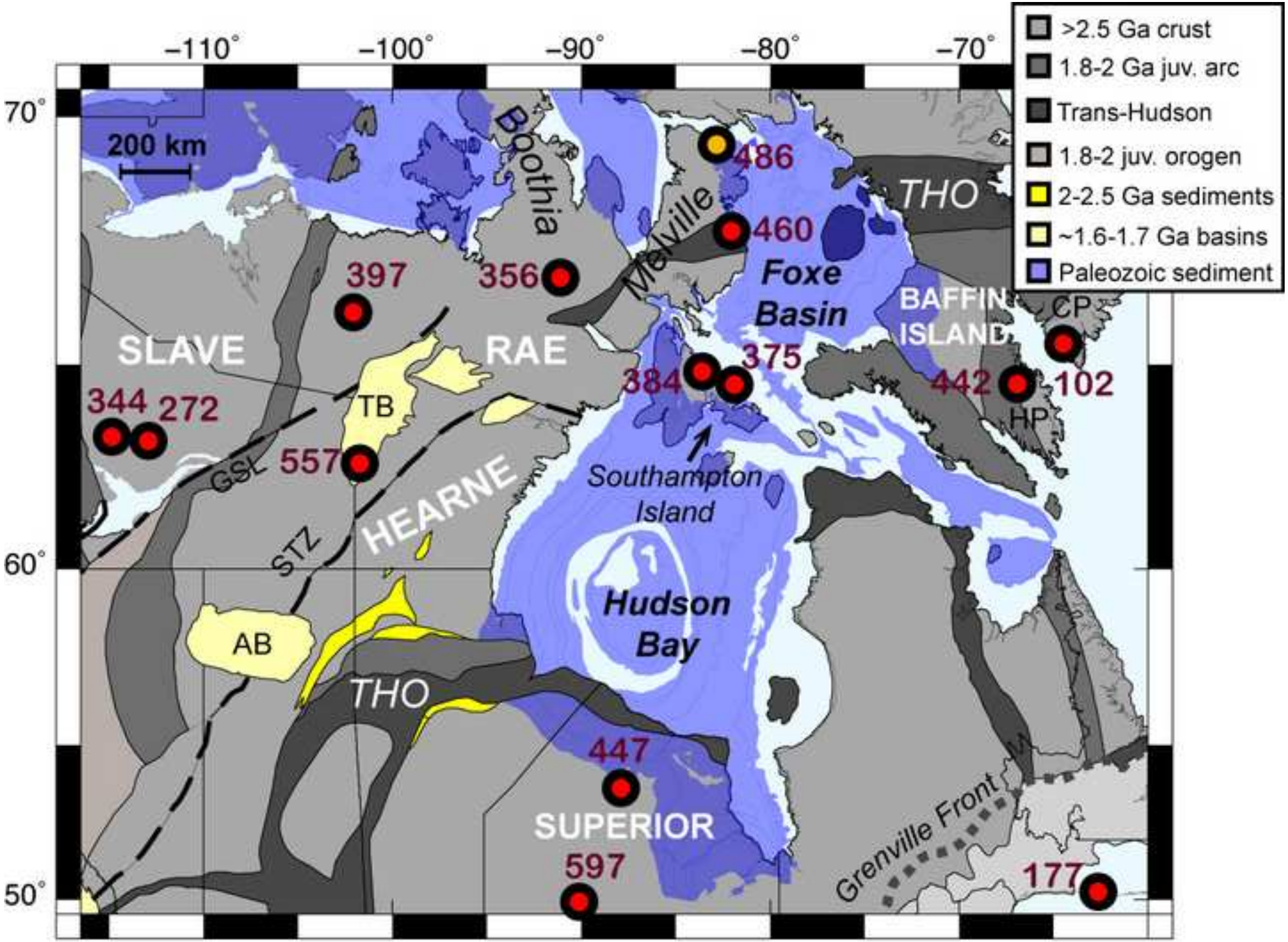

Figure2
Click here to download high resolution image

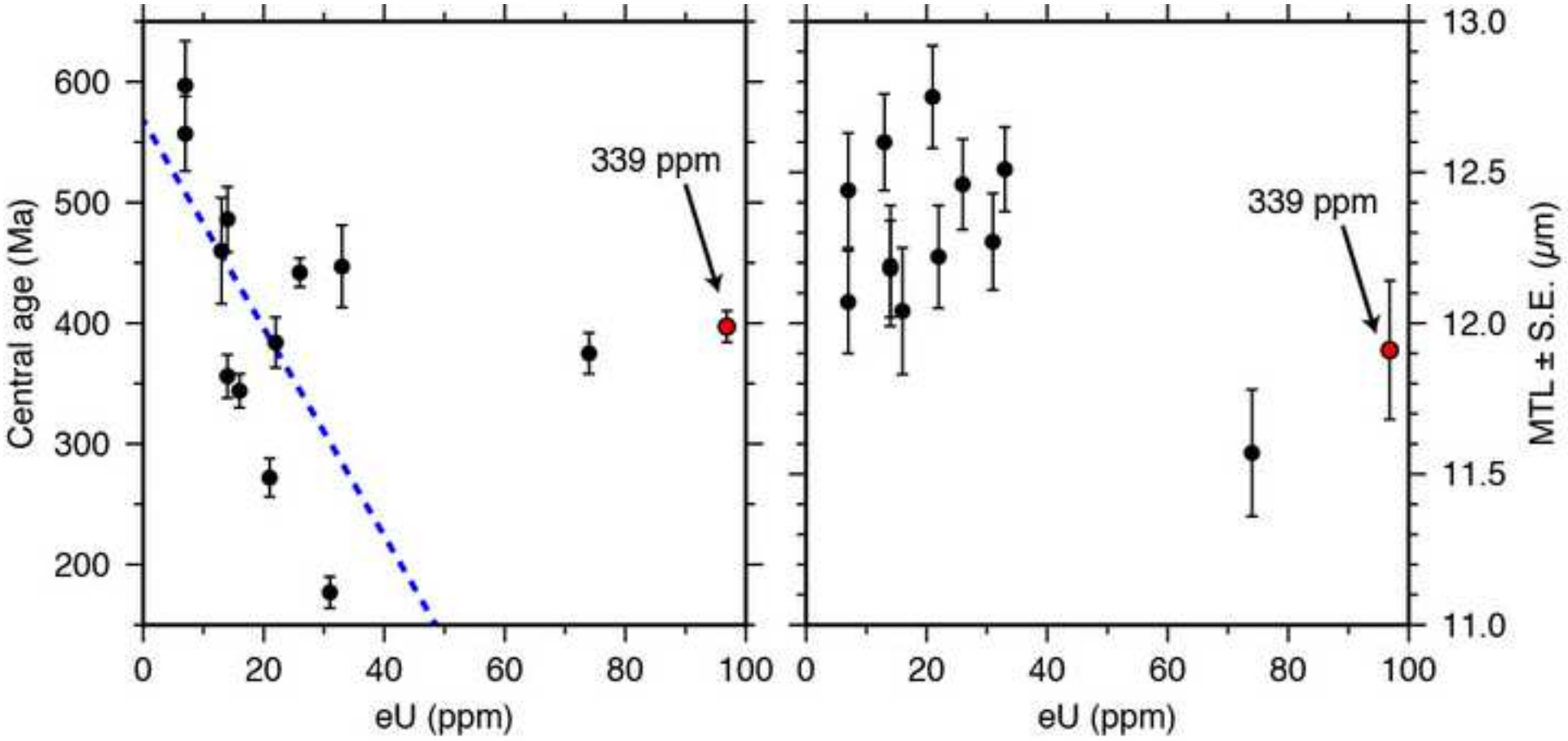

Figure3

Click here to download high resolution image

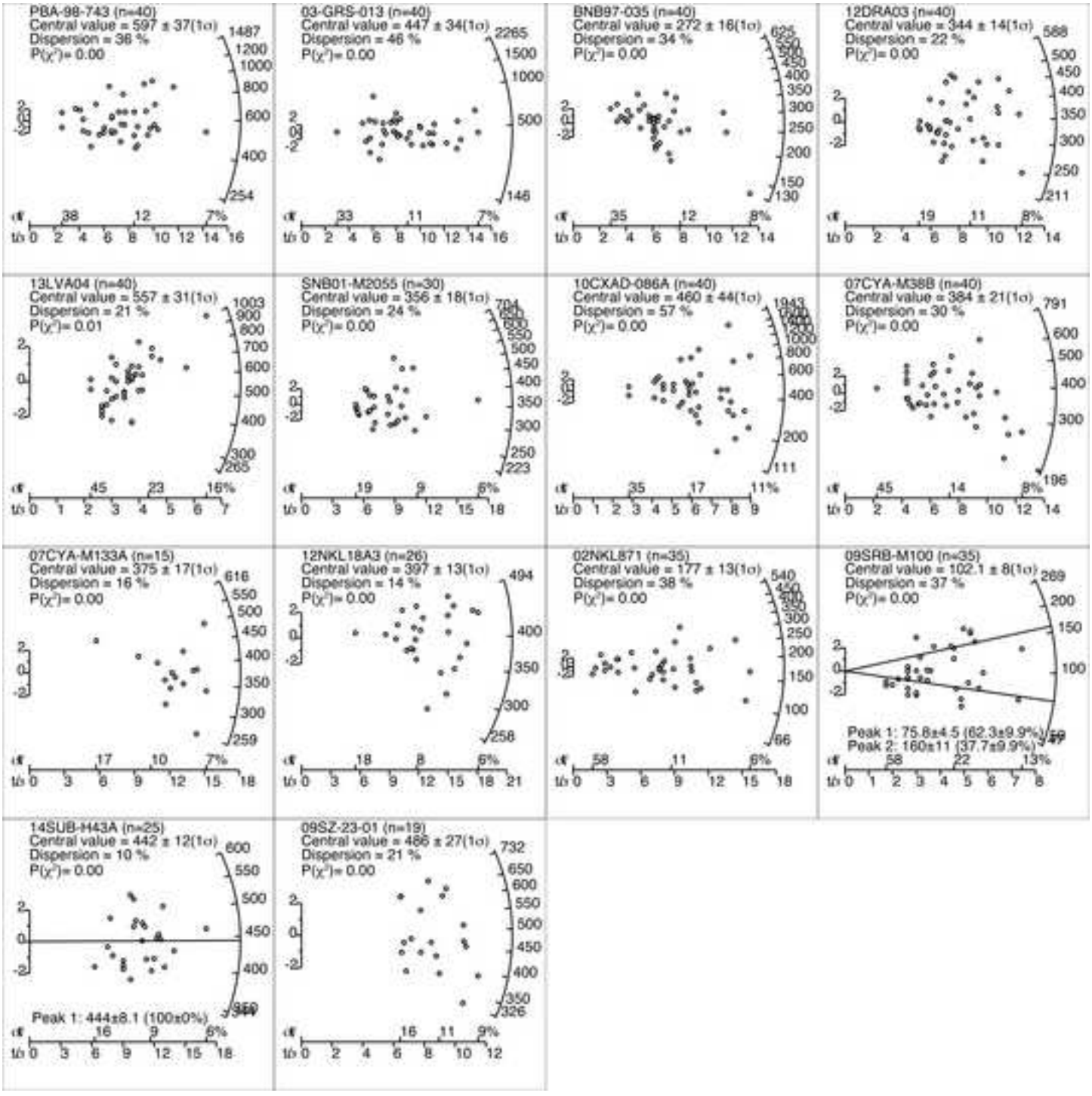

Figure4

Click here to download high resolution image

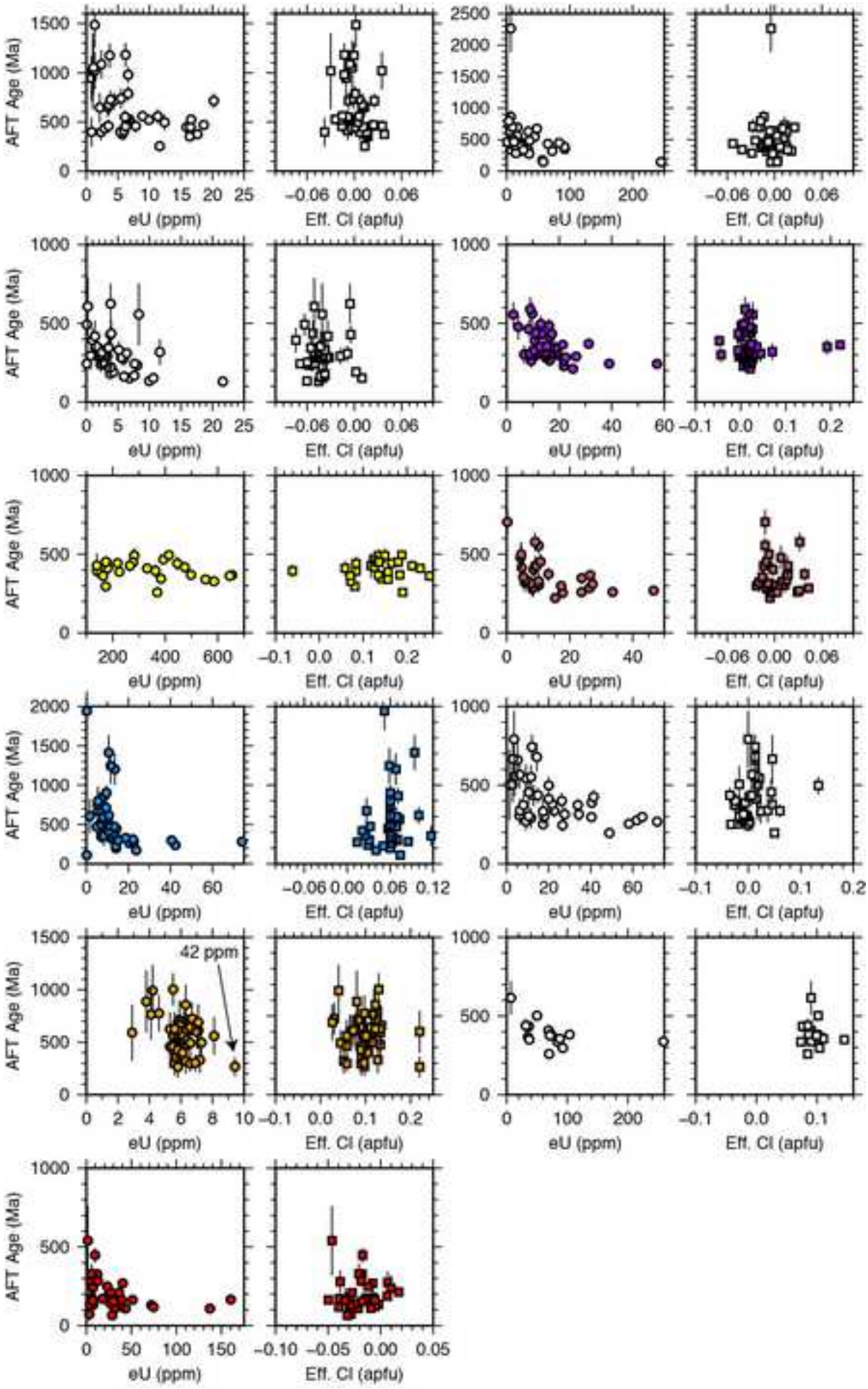

Figure5

Click here to download high resolution image

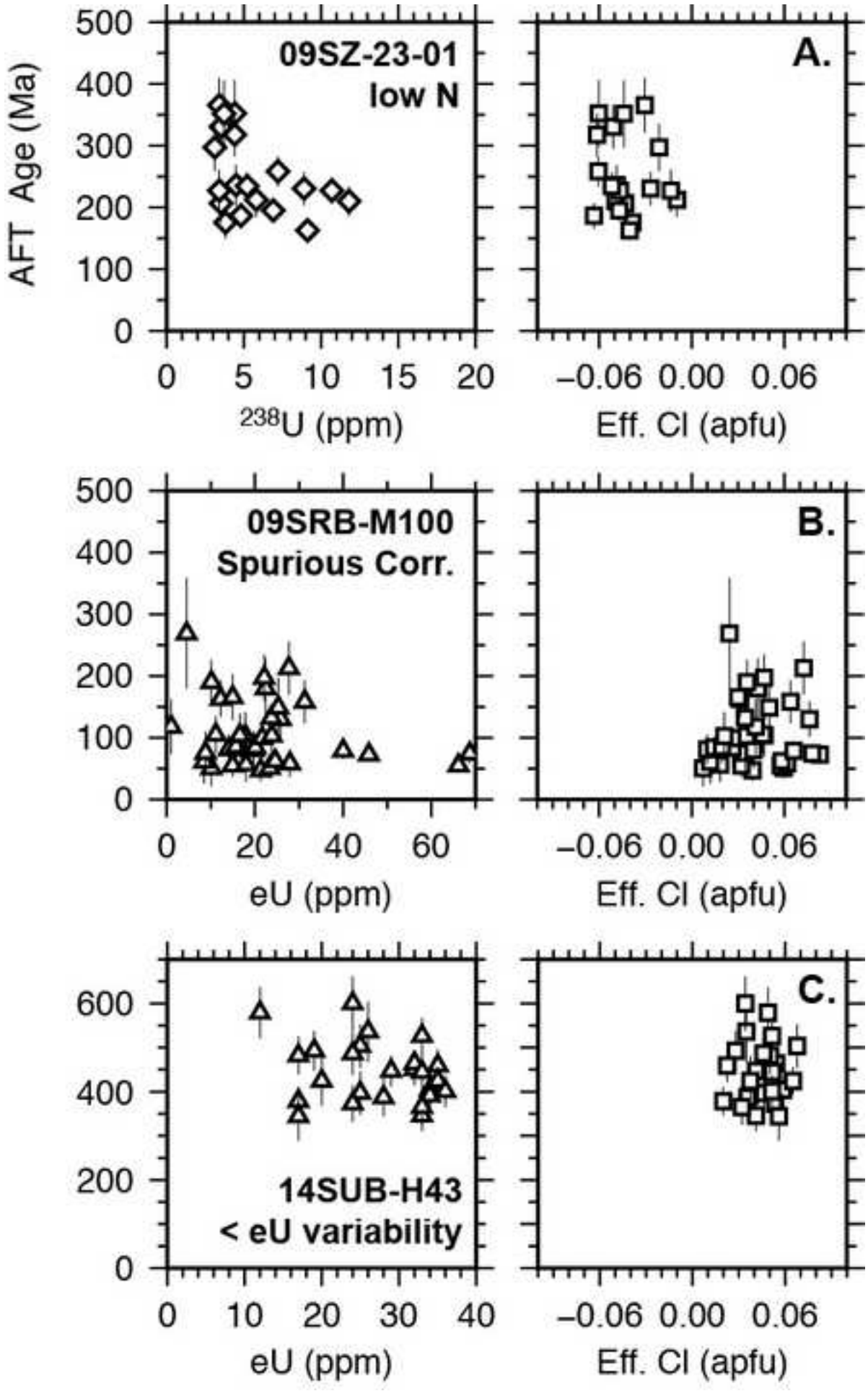

Figure 6

Click here to download high resolution image

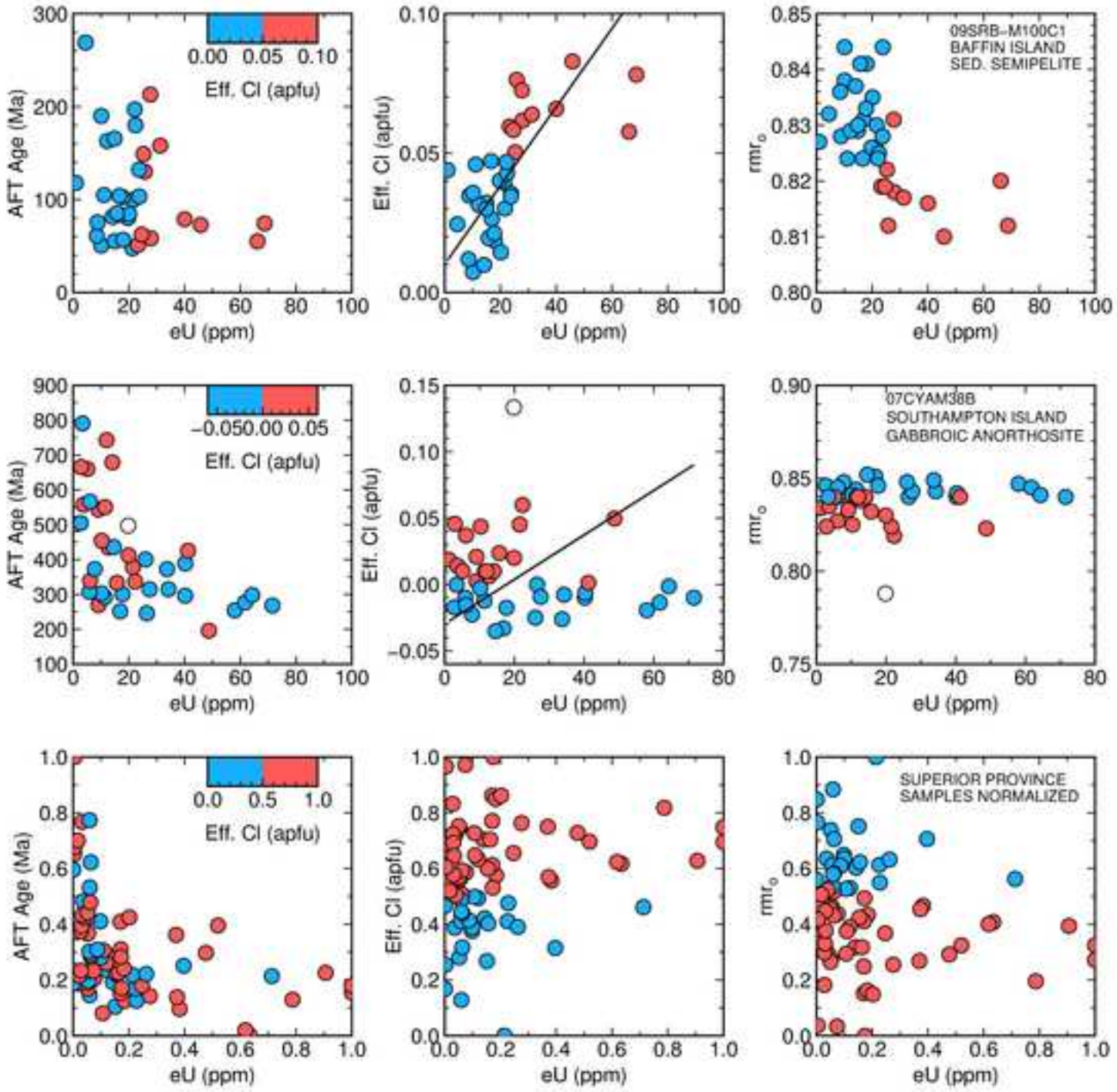

Figure 7

Click here to download high resolution image

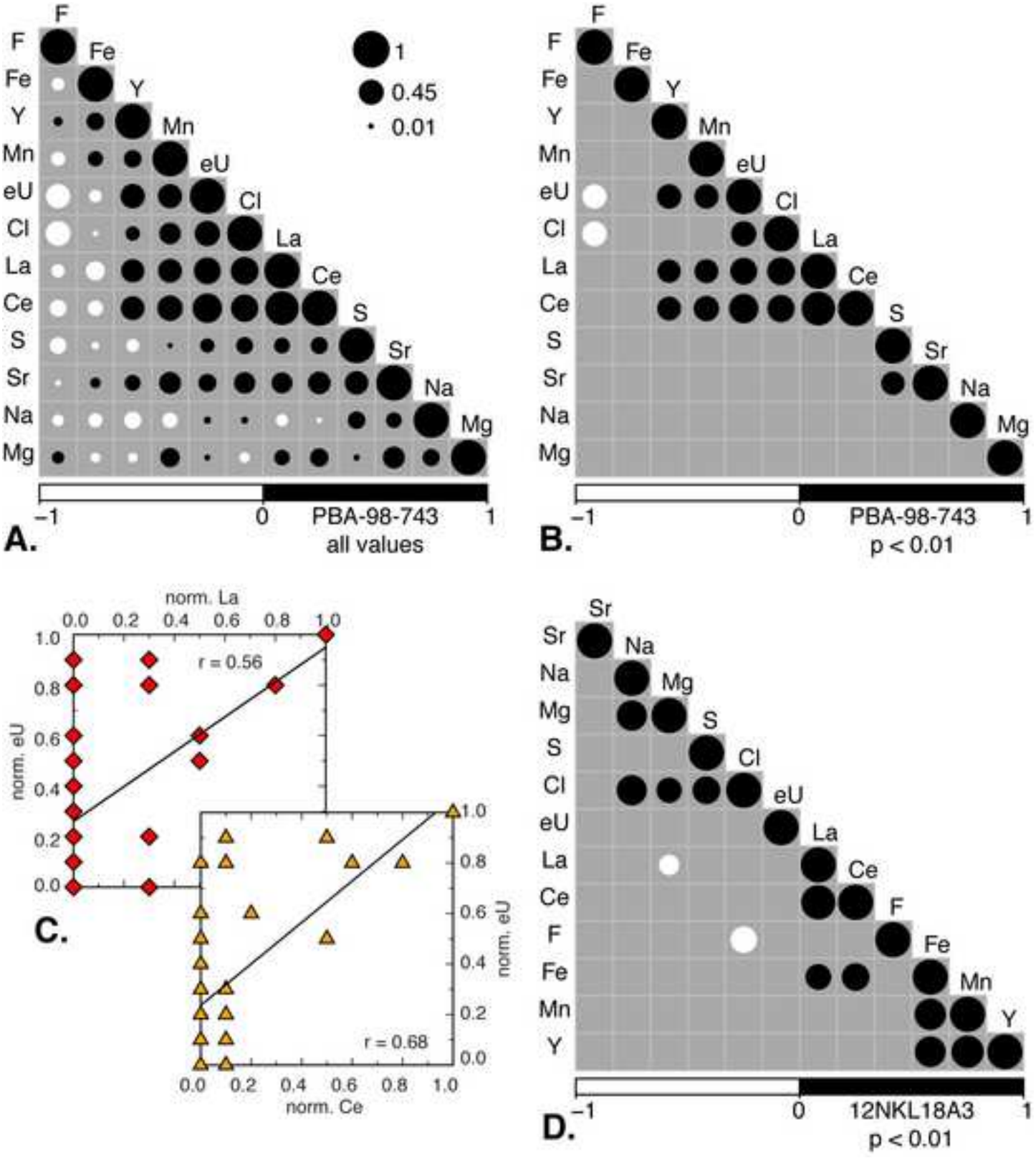

Figure8

Click here to download high resolution image

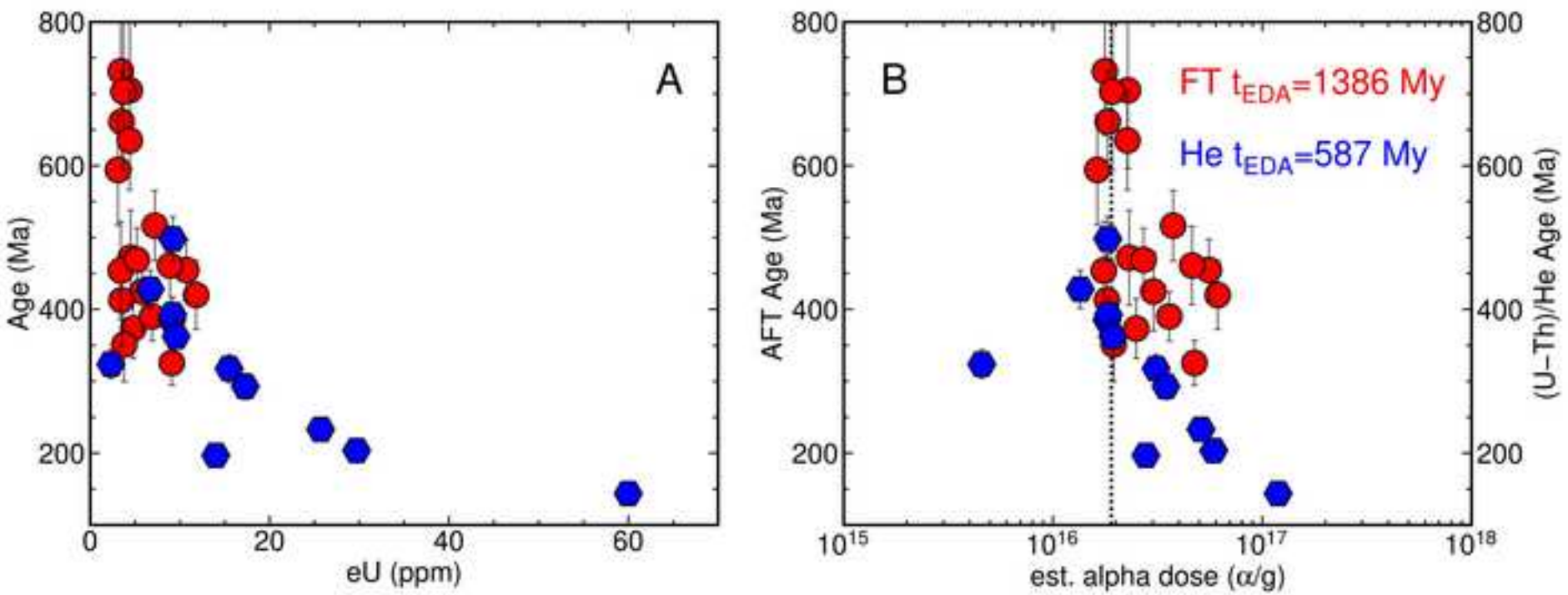

Figure9

Click here to download high resolution image